Fabrication and Mechanical Behavior of Hierarchical Architected Metamaterials

CMMI-2124826

Annual Report, Year 3

Costas Grigoropoulos (PI), Frances Allen (co-PI)
UC Berkeley

1. Research Goals

A major goal of this project to elucidate the influence of multi-photon lithography (MPL) on the mechanical properties of the photopolymerized material. To accomplish this goal, we are conducting a series of parametric studies to investigate how MPL affects the mechanical properties of the polymerized photoresist. In addition, our analysis provides insight into the plasticity mechanisms that dominate the mechanical behavior. We explore length scale effects by comparing the mechanical performance at the nanoscale with the microscale through scanning electron microscopy (SEM) microindentation experiments. Utilizing helium ion microscopy (HIM) we also investigate the effect of MPL on the fracture cross sections and on the properties of the fracture domain, including the critical fracture toughness. These analyses are utilized to construct constitutive models employed in FEA and assist in the design of multifunctional architected materials. The main objectives of the research are:

- **Objective 1:** Design, fabricate and test nanopillar structures with analysis at high resolution by TEM to investigate defect formation and agglomeration on the nanoscale as a function of the MPL fabrication parameters.
- **Objective 2:** Design, fabricate and test microstructural specimens using SEM to obtain insight into the microscopic elastic and post yield behavior. Additional characterization using HIM investigates the fractural and instability mechanisms of the material and how they manifest.
- **Objective 3:** Formulate a constitutive model that depends on the MPL fabrication parameters and can dictate the elastic, elastic unstable, post yield, plastically unstable and fracture behavior of the material, and use the model for high-precision FEA simulations.
- **Objective 4:** Design multifunctional nanocomposite architected materials with tailored micromechanical behavior.

B. Research Work

1. Augmented Multiphoton Lithography Setup

Additive manufacturing employing Multiphoton Lithography is the core manufacturing technology in this project. For that reason, our priority is the design and the implementation of new setups as well as the effective maintenance of our existing setups.

In the context of this prioritization, a new custom designed objective lens with large field of view and long working distance was designed and fabricated. In more detail, according the specifications were provided by the manufacturer, its field of view is more than 2 mm and its working distance is 20 mm. The specifications of the objective lens are explicitly presented in Table 1.1.

Working distance*	20 mm
Immersion media*	Air
Numerical aperture*	0.50
Effective focal length*	20 mm
Magnification	10 X *(with a 200 mm focal length tube lens)*
Correction collar*	0 - 1 mm cover glass thickness
Entrance pupil*	20 mm
Scanning angles*	±3°
Field of view (FOV)	2.08 mm
Primary wavelength range*	920 nm ± 10 nm
Full wavelength range	800 - 1300 nm
Anti-reflective coating	< 0.5% reflected 450-1100 nm *(per surface)*
Parfocal distance	~ 90 mm
Mounting threads*	M32 x 0.75
Weight	477 g
Group delay dispersion	~4910 fs^2 at 920 nm

Table 1.1 Technical specifications of the new objective lens

The capabilities of the new objective lens in Multiphoton Lithography were assessed in a preliminary set of experiments. For that reason, some test structures were fabricated using the existing setup that was developed during the previous academic year and employing the new objective lens. Subsequently, imaging all the structures from side view was carried out using Scanning Electron Microscopy (SEM) for determining the dimensions of the structures.

Firstly, a cantilever was fabricated for the evaluating the voxel size in the *z* axis direction. The accurate determination of the height of the voxel is critical for the success of additive manufacturing because slicing, i.e., the distance between sequent layers of a layer-by-layer structure, is determined according to the height of the voxel. If the height of the voxel is overestimated there is a risk of delamination in the structure because of pure or no connection between sequential layers. On the other hand, if the height of the voxel is underestimated, the required number of layers will increase and consequently, the duration of the fabrication can be dramatically extended. Hence, the capabilities of the objective lens are not fully exploited. According to Figure 1.1, the voxel size in z axis was measured equal to 20.4 μm. Reduction of the z-axis size can be accomplished by expanding the laser beam. This will be done in the new galvanometric setup under construction where a 5x expander will be incorporated in the setup.

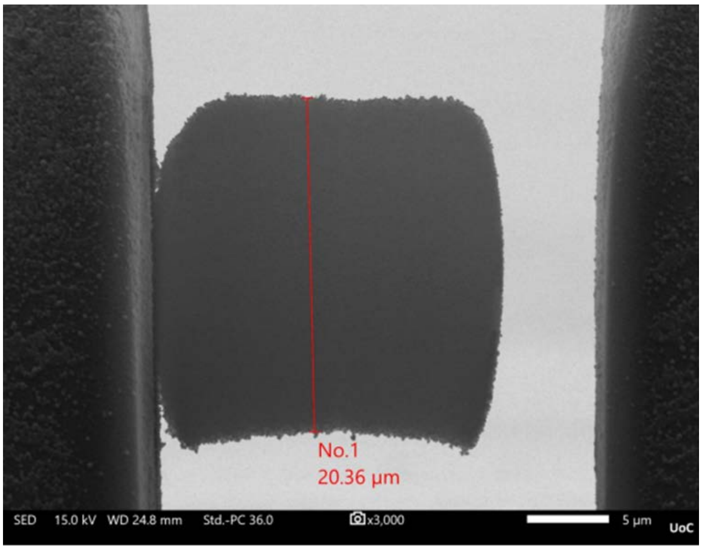

<u>Figure 1.1</u> Cantilever fabricated employing the new objective lens for experimental measurement of the z-axis voxel size

Secondly, the smoothness of curved surfaces is crucial for certain applications, such as micro-optics (Gonzalez-Hernandez et al., 2023; Stankevičius et al., 2011) and microfluidics (El-Tamer et al., 2021). For that reason, a dome was fabricated and imaged employing SEM. The smoothness of the resulted structure is considered satisfactory, as shown in Figure 1.2b.

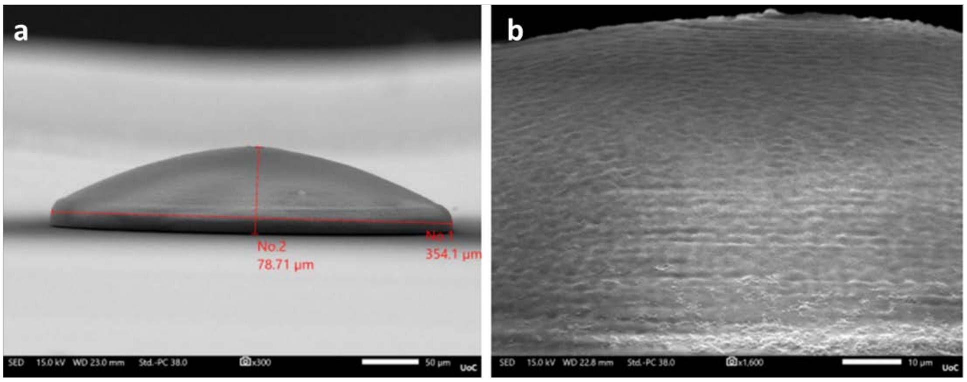

<u>Figure 1.2</u> Dome fabricated employing the new objective lens for checking the smoothness of curved surfaces: (a) Side view of the fabricated dome. The scale bar is 50 μm. (b) High magnification image of the dome surface. The scale bar is 10 μm.

Finally, the capability of fabrication of millimeter size structures was checked constructing concentric rings (Figure 1.3a) and a pillar (Figure 1.3b).

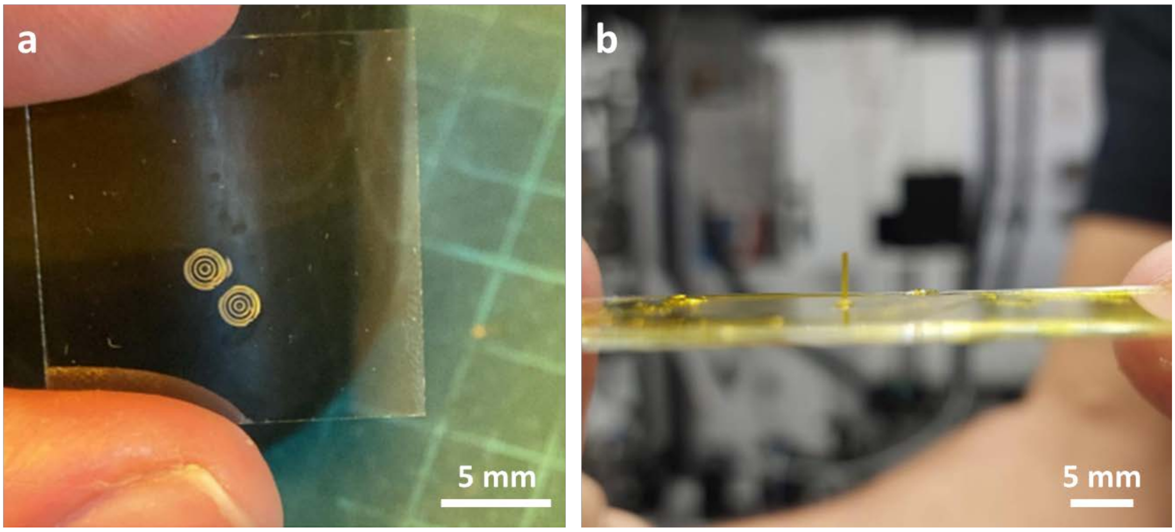

Figure 1.3 Millimeter-size structures: (a) Concentric rings where the inner diameter is 0.5 mm and the external diameter is 2 mm, (b) Pillar whose height is 4.5 mm and cross-section is 0.5 mm by 0.5 mm.

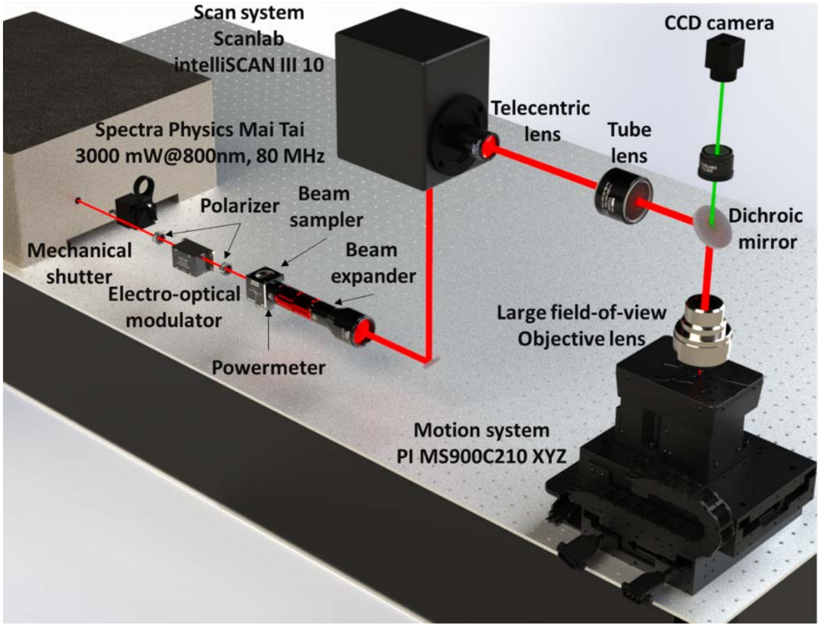

Figure 1.4 The new setup designed for maximizing the capabilities of the new objective lens.

However, using the existing setup, the capabilities of the objective lens are limited by the low laser power offered by the 100-mW Toptica FemtoFiber Pro NIR laser whose wavelength is 780 nm, pulse duration 100 fs, and repetition rate 80 MHz. For that reason, we designed a new setup where the available maximum laser power is significantly higher. This setup employs as laser source a Spectra Physics Mai Tai whose power is 3 W at 800 nm, pulse duration 100 fs, and repetition rate 80 MHz.

Moreover, laser power control is accomplished using an Electro-optical modulator and the laser power is measured using a beam-sampler where a power meter is fitted. In addition, the new objective lens is combined with a Scanlab IntelliScan III 10 for beam motion and a Physik Instrumente (PI) MS900C210 XYZ for sample motion. In this way, the large field-of-view and working distance of the objective lens are combined with an ultrafast motion system with very high resolution, high laser power, ultrafast and precise laser power control and ultrafast laser scanning offering both millimeter size working space and micrometric resolution. For maximum fabrication resolution, the diameter of the laser beam is increased by a beam expander so that the beam nearly fully covers the entrance pupil of the objective lens. The architecture of the new setup is graphically presented in Figure 1.4.

2. Biomimetic structures

The plethora of different biological systems with hierarchical nano/micro-structures constitutes an endless source of inspiration for material scientists and engineers (Yao et al., 2011). In the past couple of decades, the research was focused on understanding the physical phenomena leading to the exceptional mechanical properties of physical materials. This knowledge is succinctly ummarized in the well-known material property charts first published by M.F. Ashby (Wegst & Ashby, 2004). Recent nanotechnology advancements allow the fabrication of artificial biomimetic materials whose design is inspired by hierarchical structures of natural materials with extraordinary mechanical behavior (Yao et al., 2011).

2.1 Nacre

The hierarchy observed in natural composite materials is the source of mechanical properties that are not attainable in monolithic materials (Yaraghi & Kisailus, 2018). An excellent example is the nacre, where the assembly of weak organic and inorganic materials leads to an exceptional combination of strength and toughness. Interestingly, the high strength requirement contradicts achieving high toughness. On the other hand, while the strength, i.e., the maximum amount of stress a material can withstand before fracturing is related to brittleness, the toughness, i.e., the amount of energy a material can absorb before fracturing, is connected with ductility (Ritchie, 2011). In the case of nacre, this obstacle is surpassed by the “brick-and-mortar” architecture. In more detail, the high strength is offered by ceramic bricks and the high toughness is a result of its intrinsic toughening plasticity mechanism: the mortar acts as lubricant by allowing movement between the rigid bricks (Wang et al., 2001). Beyond these, the outstanding mechanical properties of nacre are partially a result of the parallel act of different extrinsic mechanisms: the energy absorption following the breakage of pre-existing mineral bridges between consecutive layers of bricks, the inelastic shearing between layers of bricks as a result of their surface nano-roughness and the interlocking during sliding of the aragonite pallets (Wegst et al., 2015). In addition, it should be noted that the mineral bricks are not just single crystals, but they are comprised of millions of 30-nm grains that are glued together with proteins and chitin (Li et al., 2006). All these mechanisms are illustrated in Figure 2.1.

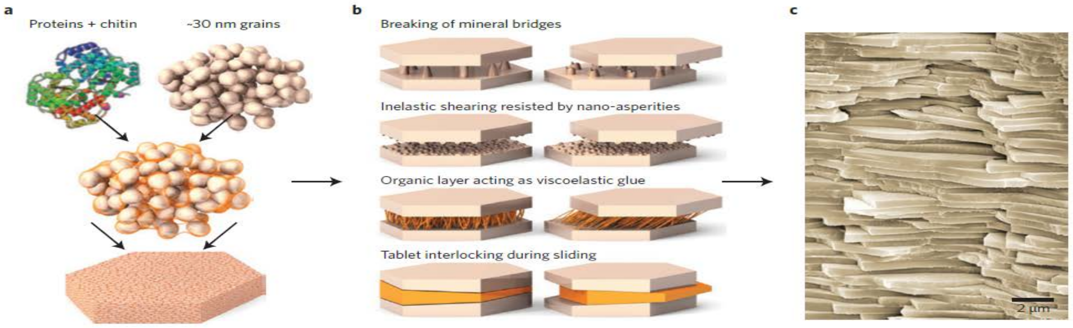

<u>Figure 2.1</u> The hierarchical structure of nacre:(a) the mineral bricks are composed of nanograins glued by a biopolymer, (b) the different toughening mechanisms which act between consecutive layers of bricks, (c) the “brick-and-mortar” structure of nacre (Wegst et al., 2015).

These features and the resulting toughening mechanisms should be considered during the design and fabrication of artificial nacre structures. Firstly, the microstructure of the mineral bricks can be expressed through the printing pattern which will be followed during the fabrication of the bricks employing Multiphoton Lithography (MPL). More specifically, the mechanical behavior of MPL-fabricated structures is affected by the sequence of additive manufacturing that is regulated by the hatching, i.e., the distance between consecutive printing lines, the hatching orientation, i.e., the orientation of the printing lines, and the slicing, i.e., the distance between consecutive layers, and the applied laser power and scanning speed (Mavrikos & Grigoropoulos, 2024b; Pertoldi et al., 2020). Secondly, during the design process, the basic geometry of the artificial nacre structure should be determined. This entails the shape and dimensions of the bricks, the distance between bricks and layers of bricks. In addition, another design variable is the potential incorporation of bridges between bricks and their dimensions. Finally, the mechanical behavior of the artificial nacre will be strongly affected by the organic biopolymer that connects the bricks and lubricates their interfaces. In our case, this biopolymeric glue will be assembled by self-organized peptide fibrils whose dimensions and number are affected by the composition of the initial solution and the self-organization conditions. A segment of the designed structure is presented in Figure 2.2(a).

Design and fabrication of a nacre-inspired structure

Because of the complexity of the brick-and-mortar structure and the corresponding features that result in the toughening mechanisms, the first trial is comprised of a simplified structure. In more detail, the structure is made of a circular plate of hexagonal bricks that are properly interconnected. For testing purposes, the whole plate is mounted on a circular frame, as it is presented in Figure 2.2(b).

Study of mechanical behavior of self-organized peptide fibrils

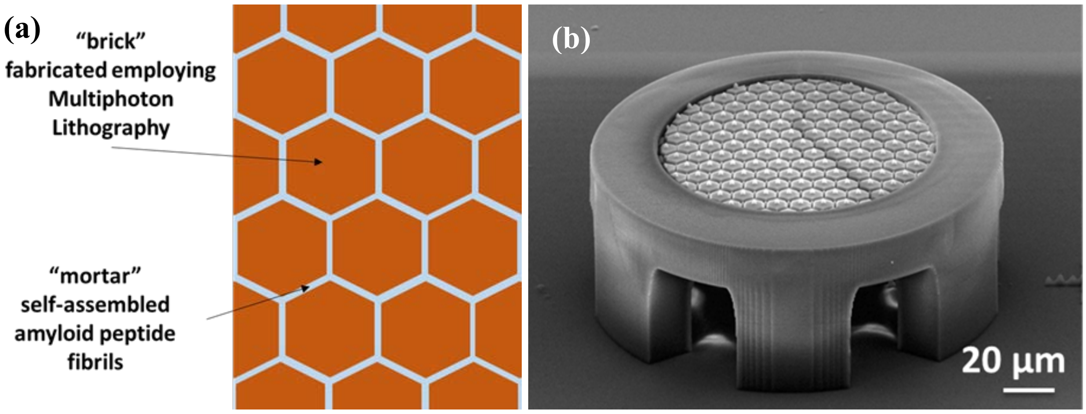

Figure 2.2 (a) Nacre-inspired structure consisting of hexagonal bricks fabricated employing Multiphoton Lithography (MPL) and biopolymeric mortar, (b) Scanning Electron Microscopy image of a nacre-inspired structure fabricated using MPL.

The mechanical behavior of self-organized peptide fibrils under quasistatic conditions was studied in the context of an integrated design process of the composite nacre structures. More specifically, the individual (Asp) aspartic residue is studied which has been shown to lead to the formation of well-ordered fibrous structures with two fluorenylmethoxycarbonyl (Fmoc) protecting groups. Many amino acid and small peptides which are modified with protecting groups self-assemble relatively fast and exhibit remarkable physicochemical properties leading to three-dimensional networks, trapping solvent molecules and forming hydrogels. For peptide fibril preparation, peptides were purchased from Bachem in the form of a lyophilized white powder of high purity >99%. Initially, a quantity of Fmoc-Asp-OFm powder was dissolved with a small amount of solvent by gentle pipetting and using an ultrasonic water bath. After the complete dissolution of the peptide by the first solvent (chaotropic solvent), the solution was removed from the water bath, and the second solvent was added to induce self-organization. The final concentration was 1 mg/ml, in a 2:8 DMSO/H2O solvent. Subsequently, a drop of the solution was deposited between two glass rods with a diameter of less than 1 mm, placed approximately 2 mm apart from each other. The drop was left at room conditions until the solvent evaporated and a peptide fibril formed, as indicated in Figure 2.3. Afterwards, a custom mechanical testing device equipped with a load cell for direct force measurement, a motorized stage for the controlled motion of the probe and a digital microscope for imaging were used.

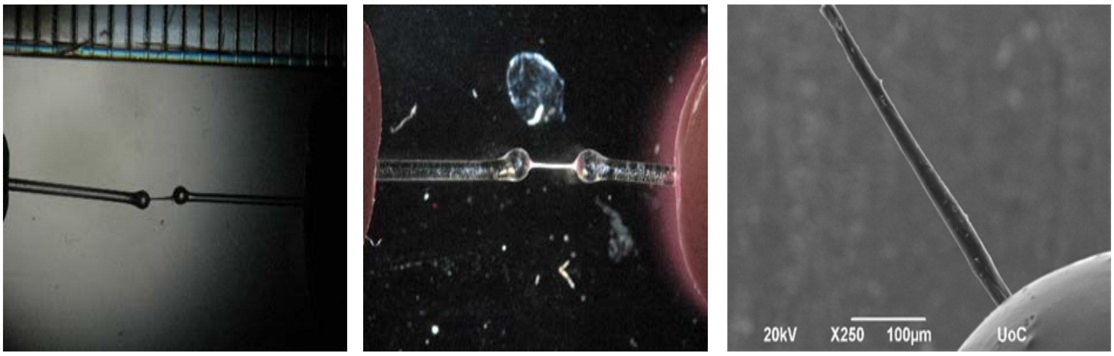

Figure 2.3 Fibril formation under stereoscope, showing the alignment of the fibers without a polarizer (left) and with a polarizer (middle), where birefringence is visible (which characterizes all forms of amyloid peptides), SEM picture of the fibril (right)

The developed mechanical testing device is illustrated in Figure 2.4. The device consists of an ultra-high resolution load cell (F329UB00A0 0.1 N by Novatech Measurements Limited) which is used for direct measurement of the applied force on the structures and a precision linear translation motorized stage (8MT173-30DCE2 by Standa) for the control and measurement of the displacement. It should be noted that the resolution of the load cell and the translation stage are 4 μN and 0.028 μm respectively. The load cell is mounted on the translational stage and equipped with a nanoindentation tip. The testing structures are firmly fixed on a linear manual translation stage with two linear degrees of freedom and a multi axis tilt platform that allow the positioning and the alignment of the structure with the tip, respectively. Furthermore, the setup is equipped with two digital microscopes that are orthogonal to each other. One of them is a low/medium-resolution digital microscope whose magnification can be set between 10x and 140x and is used for positioning while the

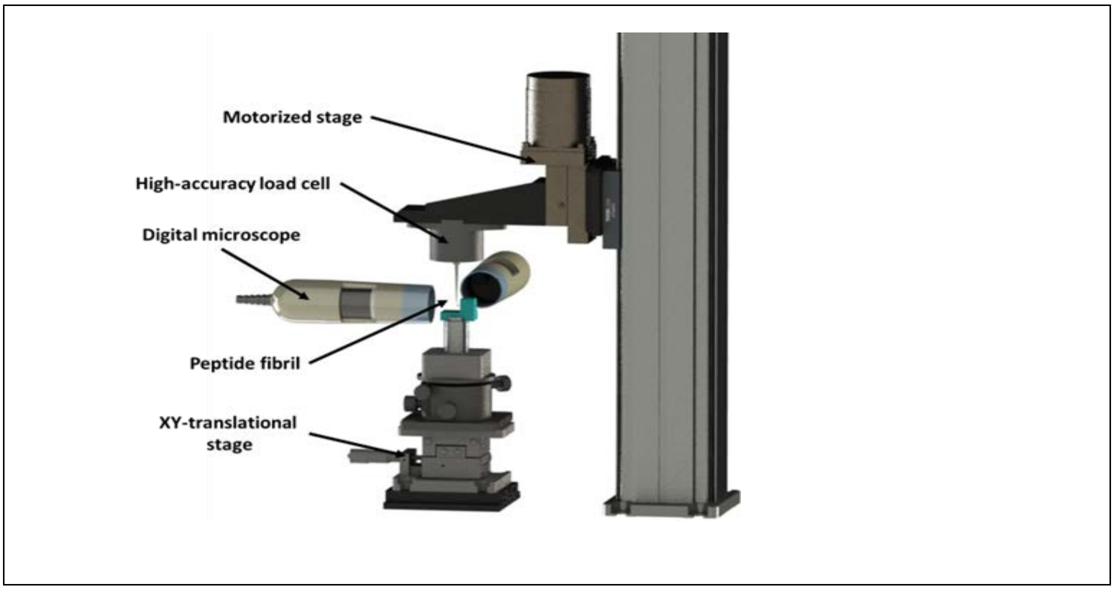

Figure 2.4. *Schematic of the custom mechanical test device*

other offers high resolution imaging as its magnification can be set between 700x and 900x and is used for the direct imaging of the compression experiments. In addition, both microscopes have the capability of video recording. In this way, we can obtain high resolution video of the experiments for further offline analysis and implement digital image correlation. The measured force-displacement curve is presented in Figure 2.5. Using the cantilever deformation equation, a Young's Modulus equal to 4.6 GPa was calculated, which directly agrees with related literature (Adler-Abramovich et al., 2018). Also, the identical elastic behavior and brittle fracture of the fibril should be noted. Using this information a constitutive model of the peptide fibrils can be easily

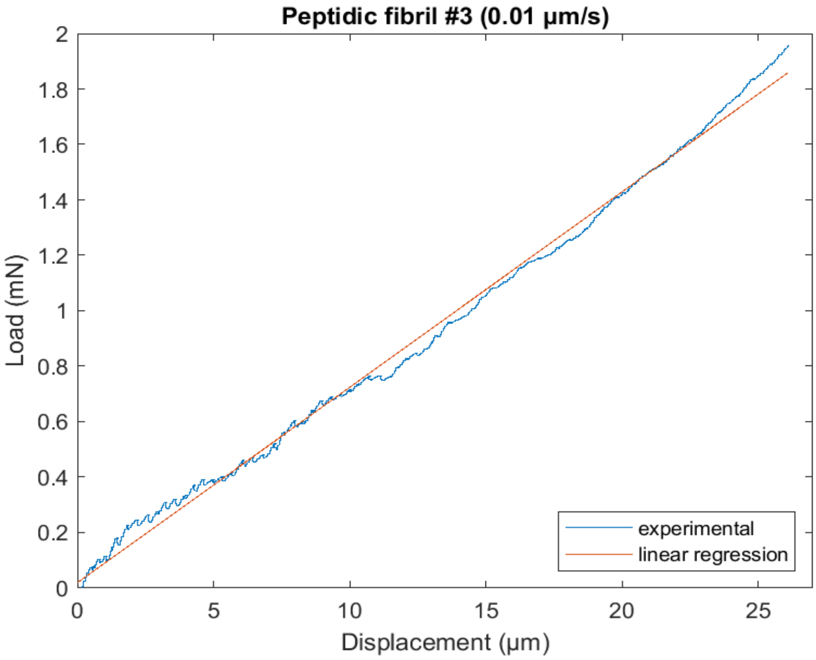

Figure 2.5 *Force-displacement curve obtained conducting bending test of peptide fibrils. The applied speed of the probe was 0.01 μm/s for quasistatic conditions to be ensured.*

obtained and used for modeling and optimization of the nacre-inspired microcomposite structures.

Optoacoustic imaging

Optoacoustic (or photoacoustic) imaging is an imaging technique based on the optoacoustic effect with various applications mainly in medicine and biology (Hutchins, 1988). In brief, the optoacoustic effect entails the generation of acoustic waves due to light absorption in the material. For this effect to occur, the light intensity must vary with time, either periodically (modulated light) or packed in a single flash (pulsed). The optoacoustic effect can be observed in vapors, gases, liquids and solids, although most applications are related to probing solid materials. In the regime of lower optical power densities, the thermoelastic expansion is the dominant mechanism and the characteristics of the generated acoustic waves are strongly affected by the optical absorption properties of the medium. If a device for acoustic wave detection is incorporated and an appropriate reconstruction algorithm applied, a photoacoustic tomography setup is developed.

Another powerful imaging technique is the confocal fluorescence microscopy, which combines the principles of confocal microscopy and fluorescence microscopy (Lavrentovich, 2012). In short, in fluorescence microscopy, the sample contains fluorophores, molecules that absorb light irradiation and emit irradiation at a longer wavelength. Hence, a fluorescence microscope uses a high-intensity light source to irradiate the sample and collects the emitted irradiation by the fluorophores, creating a magnified image of the fluorescing specimen. In the confocal mode of the fluorescence microscopy, which is also called confocal fluorescence microscopy, a three-dimensional "image" of the fluorescent specimen can be created.

Our research can take advantage of employing the combination of optoacoustic imaging and confocal fluorescence microscopy for observing the nacre-inspired composite structures. In more detail, the MPL-fabricated structure contains molecules of photo-initiator, which is employed to start the photopolymerization process. These molecules can be used as fluorophores during fluorescence microscopy. However, the self-organized peptide fibrils do not contain any fluorophores. Hence, only the MPL-fabricated structure can be imaged employing confocal fluorescence microscopy. On the other hand, the peptide fibrils can be successfully imaged using optoacoustic imaging (Cai et al., 2024). Thus, combining the capabilities of optoacoustic imaging and confocal fluorescence microscopy and taking advantage of differences of the properties of employed materials, a powerful imaging tool for interrogating nacre-inspired structures can be developed. For that reason, a hybrid fluorescence and optoacoustic microscope is used where two laser sources with different wavelengths are used and an inverted microscope are employed (Tserevelakis et al., 2023). The setup was developed in the Laboratory for Biophotonics and Molecular Imaging of the

Institute of Electronic Structure and Laser – Foundation for Research and Technology (FORTH – IESL) and is schematically presented in Figure 2.6.

The first results are very promising because high resolution imaging of peptide fibrils and MPL-fabricated structure was fully succussed, as concluded by examining the images in Figure 2.7. The optoacoustic imaging of the peptide fibrils in Figure 2.7(a) indicates the development of peptide fibrils in the inner free space of the MPL-fabricated structure and the fixation of their ends on the MPL-fabricated hexagonal pellets. Moreover, the development of fibrils around the cylindrical support post at the center of each pellet is observed. Regarding the MPL-fabricated structure, no fabrication errors are observed in Figure 2.7(b) and the designed structures were fabricated with great resolution verifying the correct choice of the design and

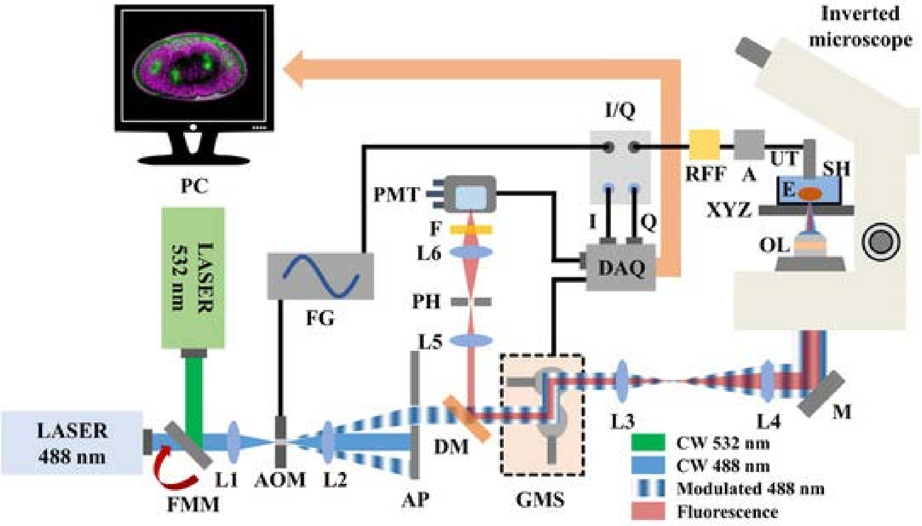

Figure 2.6 Schematic illustration of the hybrid microscopy system employed for imaging of nacre-inspired composite structures. Abbreviations: FMM, Flip mount mirror; L(1–6), Lenses; AOM, Acousto-optic modulator; FG, Function generator; AP, Aperture; DM, Dichroic mirror; GMS, Galvanometric mirror scanner; M, Broadband mirror; OL, Objective lens; E, Embryo; XYZ, Microscope's positioning and focusing system; SH, Sample holder; UT, Ultrasonic transducer; A, RF amplifier; RFF, Bandpass RF filter; I/Q, Demodulator; DAQ, Data acquisition card; PMT, Photomultiplier tube; F, Long pass optical filter; PH, Pinhole; PC, Computer.

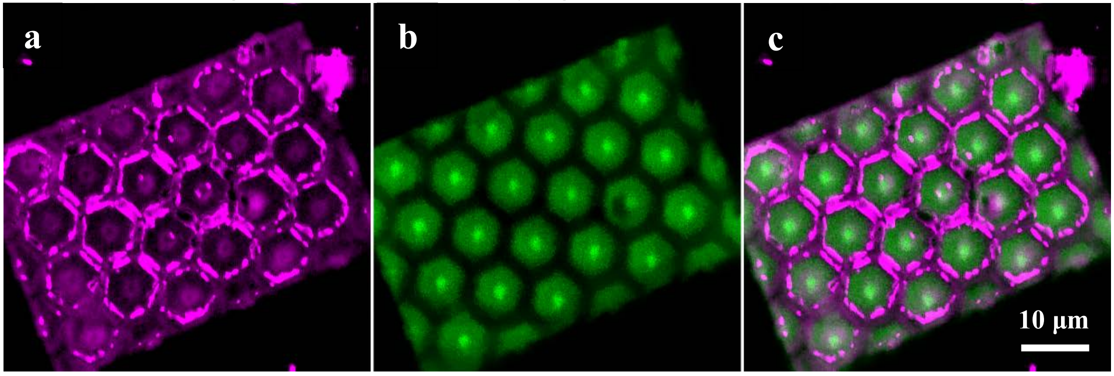

Figure 2.7 (a) Optoacoustic imaging of self-organized peptide fibrils (b) Confocal fluorescence microscopy imaging of Multiphoton Lithography (MPL) fabricated structure (c) Combination of images (a) and (b).

fabrication parameters. Finally, Figure 2.7(c) consists of an image of the micro-composite structure.

Impact analysis of MPL-fabricated structures

The most interesting characteristics of nacre are its extremely high toughness and ductility. Hence, studying the toughness and energy absorption of MPL-fabricated structures is essential for the design and modeling of nacre-inspired micro-composite structures. The Laser Induced Forward Transfer (LIFT) technique was employed for examining the behavior of the fabricated structures upon impact. LIFT is based on the interaction between light and matter, wherein light is absorbed by a metal or polymer film on the donor substrate and converted into internal energy (Serra & Piqué, 2019). When a laser beam is focused on the film through a transparent substrate, this causes temperature rise and bubble formation. Subsequently, the bubbles expand and collapse, triggering the formation of a jet that accelerates the projectile material.

For the current experiments, a thin layer of cyanoacrylate glue was coated on glass microscope slides using an adjustable micrometer film applicator, set at a blade height of ~50 µm. The cyanoacrylate glue served a dual function: it acted as both the bonding layer between the glass microscope slide and the aluminum foil, and as a dynamic release layer (DRL). The aluminum foil, with a total thickness of 15 µm, was placed on top of the cyanoacrylate glue layer. The donor substrate was then laser-patterned with circular outlines to aid in the transfer of material (outer diameter 120 µm, inner diameter ~75-80 µm). The patterning was carried out in an array of 30 x 10 spots. Using an appropriate imaging setup, including a high-speed camera with a recording speed of up to 60,000 fps, the projectile velocities before and after impacting the tested structures were measured for different laser energy densities. With varying laser powers, projectile speeds between 45 and 160 m/s were achieved. By measuring the speed of the projectile foil after impact and observing how the structures were damaged and/or absorbed the energy of the collision, interesting results emerged regarding the toughness of the different structures and how each type of structure absorbs the foil's kinetic energy. The

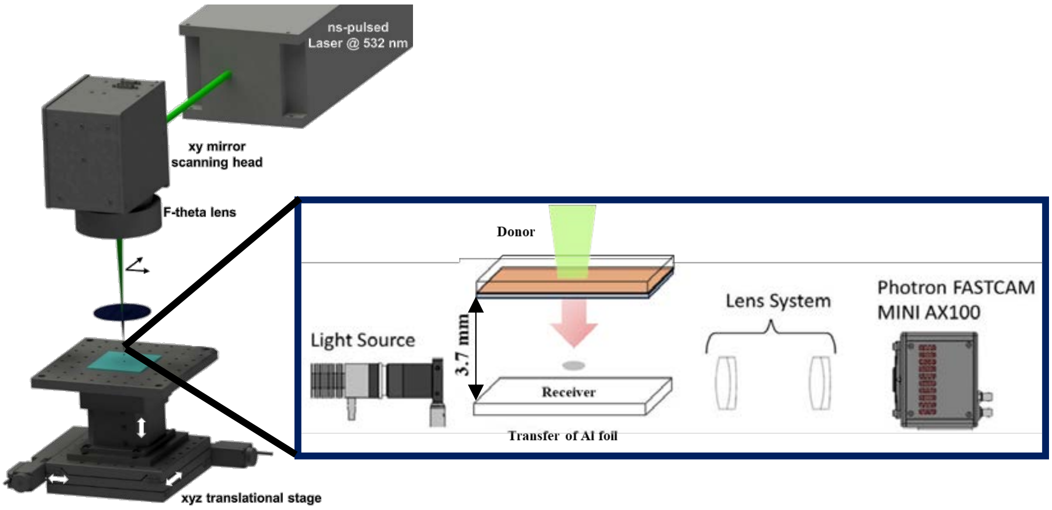

Figure 2.8 The employed Laser Induced Forward Transfer (LIFT) setup where a green laser beam and a scanning head are employed, and an appropriate imaging system is integrated for the projectile recording. The imaging system consists of a light source, a lens system and a high-speed camera.

tested structures included a solid cube, a woodpile structure, and a lattice structure. The employed setup is presented in Figure 2.8.

A simulation model of the mechanical behavior of MPL-fabricated structures under high strain rates based on the above experimental data was developed. In more detail, the simulation was conducted in LS-Dyna, a finite element code designed for large deformations and successfully used for impact analysis in many studies (Barauskas & Abraitienė, 2007; Singh & Singh, 2015). The aluminum foil was simulated utilizing 3D solid elements using a plastic strain-based failure material model under piecewise linear plasticity. The simulation of the MPL-fabricated structures were carried out employing 3D solid elements and the power-law plasticity model combined with the Cowper-Symonds model for strain rate accounting (Cowper & Symonds, 1957; Matache et al., 2019). The applied constitutive law is:

$$\sigma_y = K \cdot e^n \left[1 + \left(\frac{\dot{\varepsilon}}{C} \right)^{\frac{1}{p}} \right] \qquad (2.1)$$

where σ_y is the yield stress, e the real (logarithmic) strain, K is the strength coefficient, n is the hardening coefficient, $\dot{\varepsilon}$ is the stain rate, C and p are the Cowper-Symonds coefficients. The above material model is applied in the LS-Dyna simulation using the MAT_POWER_LAW_PLASTICITY (MAT_018). The material model was applied both for the MPL-fabricated structures and the projectile. The appropriate selection of the values of the parameters of material model of the projectile was based on the literature (Bal et al., 2019). Two snapshots, one before and one after the first contact between the projectile and the cube, developed simulation are present in Figure 2.9(a-

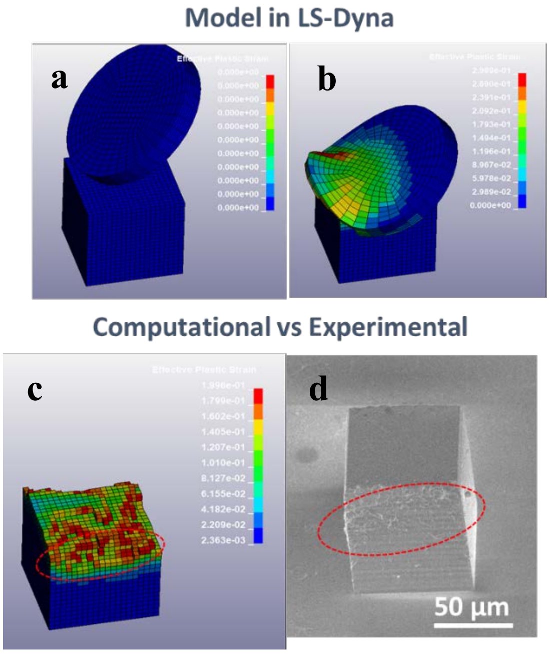

Figure 2.9 (a) The initial snapshot of the developed simulation, (b) Simulation snapshot where the projectile is in contact with MPL-fabricated cube, (c)MPL-fabricated cube after the collision, (b) Scanning Electron Microscopy image of MPL-fabricated cube after impact experiment

b). The final snapshot of this simulation, which is shown in Figure 2.9(c), presents excellent qualitative convergence with the Scanning Electron Microscopy image (Figure 2.9d) of the corresponding experiment.

2.2 Diabolical ironclad beetle

The diabolical ironclad beetle is an intriguing organism from the mechanical behavior standpoint due to the exceptional toughness of its elytra (Rivera et al., 2020). A suture with a particular geometry at the higher point of the elytron (Figure 2.1a) allows large displacements of the elytron without fracture, thanks to high degree of interdigitation (Olberding, 2021). Geometric interlocking mechanisms can delocalize strains and, in this way, the fracture toughness is increased (Mirkhalaf & Barthelat, 2017). In more detail, the fracture of a suture might happen because of suture pullout or tab fracture (Malik & Barthelat, 2018). On one hand, the structure can experience larger displacements, absorbing higher amount of energy, where the fracture mechanism is the suture pullout, leading to a more ductile and tough structure. On the other hand, tab fracture is observed at more brittle and stiff structures (Malik & Barthelat, 2018). Hence, the introduction of a suture can lead to a ductile structure, even though the used material is brittle (Malik et al., 2017). Moreover, another factor to control the mechanical behavior and fracture mechanism of sutured structures is the coefficient of friction between the surfaces of the suture, with higher coefficient of friction having as a result of the increase of the pullout force (Malik & Barthelat, 2018). Regarding the elytron of diabolical ironclad beetle, simulations concluded that the protein layer between the surfaces of the median suture acts as "lubricant" decreasing the pullout force and preventing tabs fracture (Malik & Barthelat, 2018). In addition, the elytron is composed of layers of stiff inorganic material that are connected to each other with layers of chitin, thereby increasing the compliance of the material (Rivera et al., 2020).

The blades of the median suture of the diabolical ironclad beetle can be modeled using three identical ellipses, as it is illustrated in Figure 1b. This model utilizes three design variables: the length of the major axis of the ellipse, the ratio between the major and the minor axis of the ellipse and the interlocking angle. It should be noted that the use of the ratio between the major and the minor axis instead of the length of the minor axis is preferable as the mechanical behavior is affected by the ratio between both axes and

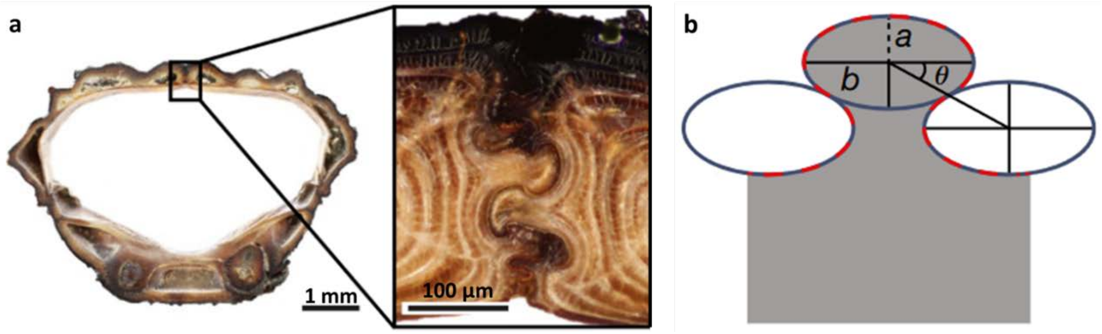

Figure 2.10 (a) The toughness of the elytron of the diabolical ironclad beetle has attracted the attention of the research community. The main reasons of the extraordinary mechanical performance are: (i) the geometry of the medial suture of elytron, (ii) the multilayer structure of the material and (iii) the connecting material between the suture sides that acts as a lubricant. (b) the proposed modeling of the suture (Rivera et al., 2020).

not merely the length of each axis (Wickramasinghe et al., 2023). Also, the gap between the suture surfaces is a design variable. Finally, as in the case of nacre, hatching, hatching orientation, slicing, laser power and velocity should be taken into account.

Design and fabrication of a hinge

Drawing inspiration from the modeling that is presented in related literature (Rivera et al., 2020) , the hinge was modeled by ellipses. Firstly, the contour of the inner and outer parts was determined. Subsequently, lines at constant distance from the contour were designed until the whole area was hatched. The distance between the lines was set to 2.4 μm. Then, the resulting lines were discretized in straight segments, whose maximum distance from the related curve is 0.02 μm, and the maximum angle between two consecutive segments is 5°. For the track design, the analytical equations were numerically solved in MATLAB applying suitable boundary conditions.

For a proof-of-concept purpose, a hinge was fabricated on a glass substrate. In Figure 2.11, the designed tracks are presented, Video 1 shows the fabrication process as recorded by the CCD camera of the MPL system, and, in Figure 2.12, a Scanning Electron Microscopy (SEM) image of the fabricated hinge is presented. According to the video, the thickness of the printed lines is constant and no material destruction is observed as the amplitude of the speed was constant on the same line. However, shrinkage during the development process was significant, according to Figure 2.12.

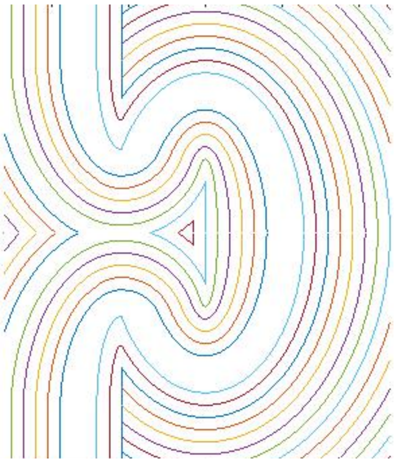

Figure 2.11 Designed tracks

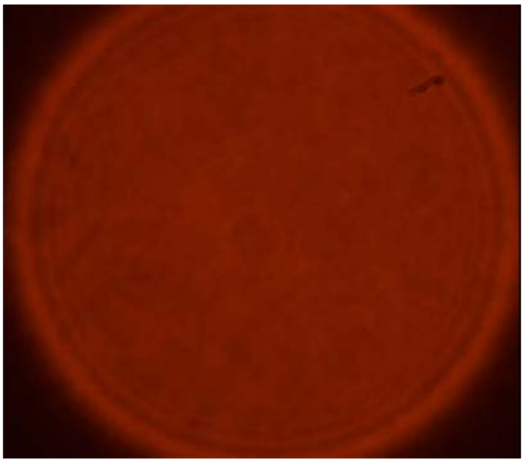

Video 1 Fabrication process of the hinge
[*https://drive.google.com/file/d/1QoGgTcnyilFdLHzHMwICgzm1MXpWwVtO/view?usp=drive_link*](https://drive.google.com/file/d/1QoGgTcnyilFdLHzHMwICgzm1MXpWwVtO/view?usp=drive_link)

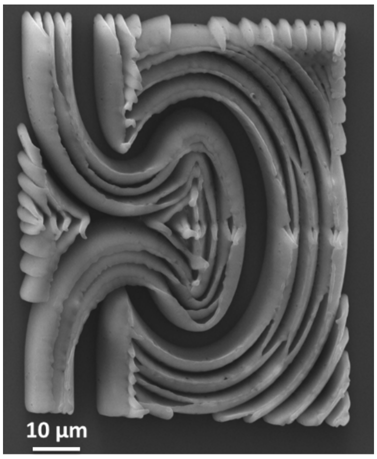

Figure 2.12 Scanning Electron Microscopy (SEM) image of the fabricated hinge

Failure simulation

This work suggests means to estimate the material properties of MPL-fabricated structures based on an iterative feedback simulation procedure using LS-Dyna (Mavrikos & Grigoropoulos, 2024a). These material properties can be used for the simulation and design of structures that include complex features. Consequently, the experimental trials and the related duration of the design process can be dramatically decreased, increasing the efficiency and productivity during the design. The proposed approach is demonstrated in the design and simulation of complex geometries, inspired by the Phloeodes diabolicus. Finally, while related simulations reported in the literature were limited to the elastic regime, this work shows that simulation of failure of complicated geometries under complex loading conditions is feasible.

For simulation validation, a double-fixed beam whose length was 50 μm and its cross-section 30 μm by 10 μm was fabricated. The beam was supported on either side by two towers whose cross-section was sufficiently larger than the cross-section of the beam. The entire structure was sliced by setting the distance between two adjacent lines in the same layer at 0.4 μm and the distance between two consecutive layers at 0.8 μm. The laser power was set at 11 mW and the scanning speed was 3000 μm/s.

The failure of a double-fixed beam is simulated and the simulation is experimentally validated following an iterative feedback simulation process. According to Figure 2.13, qualitative convergence between experiment and simulation is observed. Figure 2.14 further demonstrates quantitative convergence.

Subsequently, two complex designs, inspired by the Phloeodes Diabolicus, are simulated. The first one, shown in Figure 2.1, included five identical hinges. In Figure 2.1, the simulated failure of the structure is presented. As the failure was caused by a fracture at the first hinge, in the second design, which is presented in Figure 2.1, the hinges are not identical, but their size increases as the distance from the upper surface of the beam decreases. According to the results of the simulation which are presented in Figure 2.16, in the second design, fracture was observed in multiple regions. The limit load of the two designs is almost the same, but the displacement when the failure has occurred is higher in the second design, as concluded by the force-displacement curves which are presented in Figure 2.19.

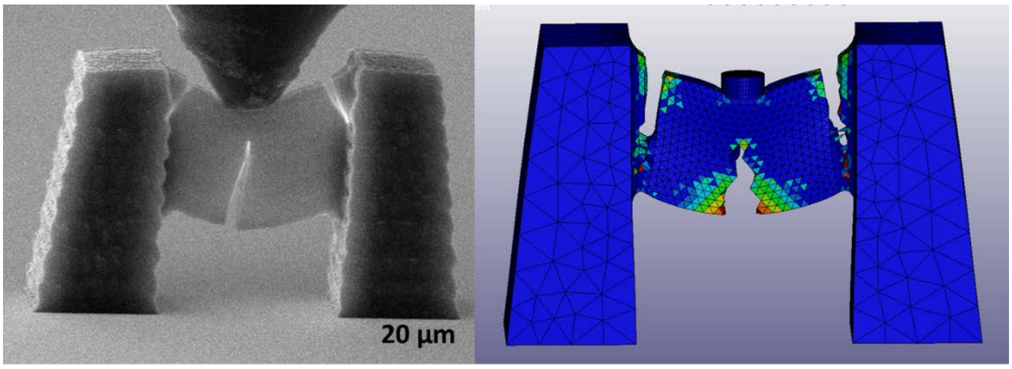

Figure 2.13 Failure of a double-fixed beam as it experimentally occurred (left) and as it is simulated using an iterative feedback simulation process in LS-Dyna (right).

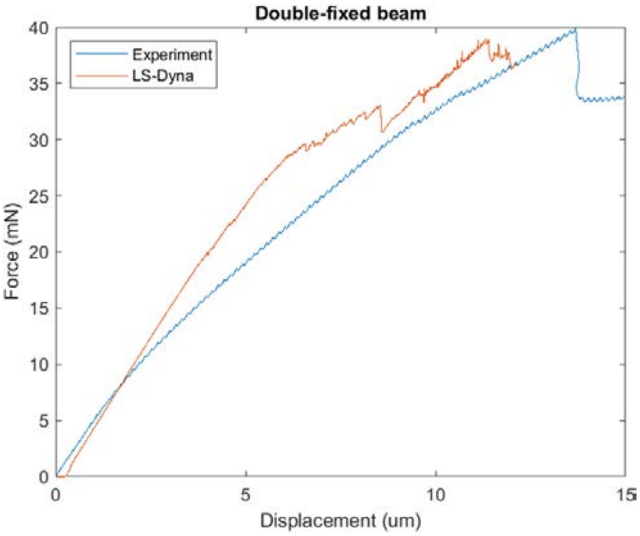

Figure 2.14 Force-displacement curves as they are obtained by experiment and simulation.

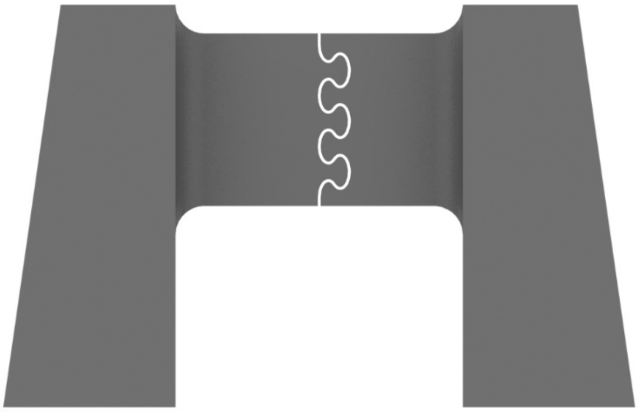

Figure 2.15 *A connection, inspired by Phloeodes Diabolicus, with multiple identical hinges.*

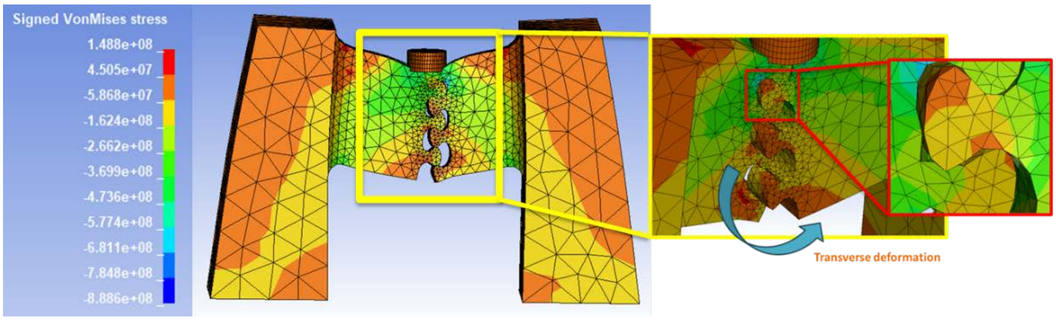

Figure 2.16 *Von Mises stresses during fracture (in Pa). Transverse deformation of the two parts of the beam is observed during the fracture. Fracture first comes at the first hinge.*

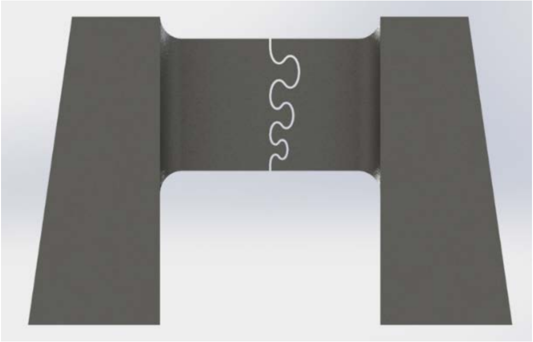

Figure 2.17 *A connection, inspired by Phloeodes Diabolicus, with multiple hinges whose size increases as their distance for the upper surface decreases.*

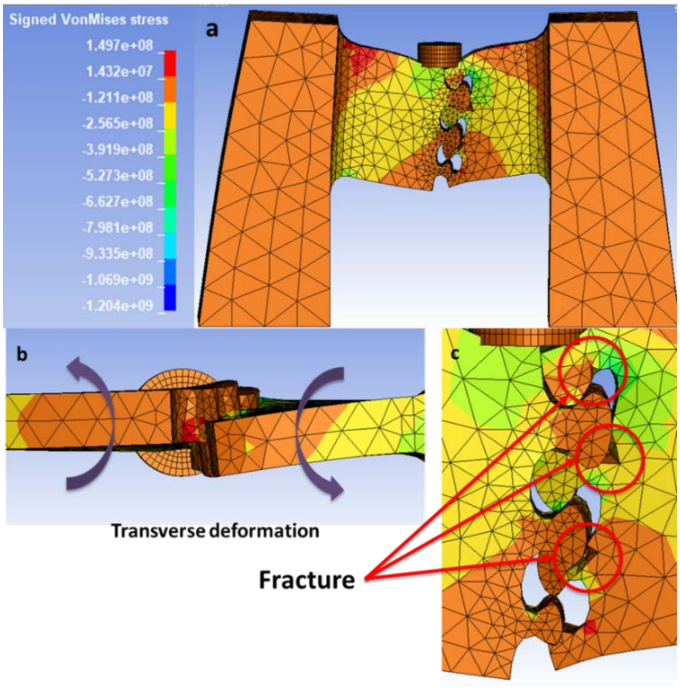

Figure 2.18 *Von Mises stresses during failure (in Pa) of the second design. (a) Simulated deformation of the second design during failure, (b) Transverse deformation of the two parts of the beam is observed during the failure, (c) Detail where multiple regions of fracture are observed during failure.*

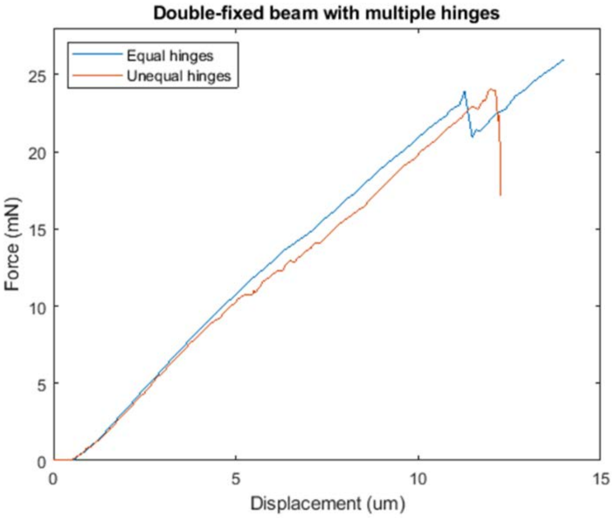

Figure 2.19 *Force-displacement curves of the two simulated designs*

Application of Limit Analysis on MPL-fabricated structures

The limit analysis consists of a structural analysis field committed to developing efficient methods to directly determine estimates of the collapse load of a given structural model (Chen & Han, 2007; Neal, 1977). For that reason, limit analysis is based on a set of theorems, referred to as limit theorems, which are based on the law of energy conservation. The limit analysis offers economical and rational designs and its computational cost is almost zero as it is an analytical method. It is an ideal method when avoiding plastic collapse is the governing design criterion. However, it cannot be applied in brittle or fatigue failure or in buckling problems. The main assumptions are that the deformations are small, that plane cross-sections remain plane and the existence of an ideal relationship between stresses and strains. Moreover, residual stresses, axial forces and shear forces are ignored. In addition, the flexural modulus is considered equal to the Young's Modulus, which is the same in tension and in compression.

The motivation for applying limit analysis on MPL-fabricated structures comes from seeking a low-cost process for the initial design and decrease of the design space. The theory of limit analysis is an ideal solution as it is analytical, computationally inexpensive and offers sufficient accuracy for our needs. The experimental curve in Figure 2.14 was used as a case study. The experimental collapse load is 39.6 mN and the estimated collapse load employing limit analysis is 41 mN. The relative error between the experimental and the estimated collapse load is 3.5%. Hence, limit analysis can be successfully applied to MPL-fabricated structures and can facilitate very fast initial designs and dimensioning structures when the main design criterion is maximizing the total collapse load.

3. Study of Helium-Ion-Irradiated Multiphoton Lithography Fabricated Structures

Localized ion irradiation using the nanometer-sized ion beam of the Helium Ion Microscope (HIM) has recently emerged as a versatile tool for tuning material properties, such as electrical and thermal conductivity, and for modifying surface topography on the micro to nanometer scale (Allen, 2021).

Our research is focused on studying the behavior of Multiphoton Lithography (MPL) fabricated structures irradiated with helium ions employing the HIM. The material used is SZ2080, a hybrid ceramic-polymeric photopolymerized material. In the literature, very different helium ion irradiation effects have been reported for ceramics versus polymers. For example, in the case of silicon, helium ion induced swelling due to nanobubble formation can occur (Livengood et al., 2009), whereas in the case of polymers, shrinkage due to cross-linking and compaction can arise (Tavares 2020). This makes helium ion irradiation of the ceramic-polymer SZ2080 composite an interesting system to study.

For these experiments, cantilever structures such as the one shown in Figure 3.1(a) were fabricated by MPL. These cantilevers were connected to a rectangular structure (right hand side of the image), also fabricated by MPL. The rectangular structures were fabricated employing galvanometric mirrors for high speed (lower accuracy), whereas the cantilevers were fabricated using three nanometric stages for higher accuracy (lower speed). Then, a small area close to the fixed end of cantilever was helium-ion irradiated to a dose of 5e16 ions/cm^2. The angle between the incident ion beam and the substrate surface normal was approximately 17°. The result of this irradiation was bending of the cantilever, as shown in Figure 3.1(b). Next, a second irradiation (same dose and area) was performed further along the length of the cantilever. This resulted in a second bend, as shown in Figure 3.1(c). At first glance, material removal causing notch features at the irradiation sites could be inferred. In order to determine whether such material removal could be responsible for the bending, a second cantilever was irradiated with gallium ions, which have a significantly higher sputter yield than helium and are widely used for the thinning of specimens for Transmission Electron Microscopy (TEM) (Orloff et al., 2003). However, as shown in Figure 3.2, material removal by milling did not result in a bending action. Hence, we infer that the notches and bending observed for the helium-ion-irradiated MPL-cantilevers is due to local shrinkage from ion-induced scission and subsequent cross-linking of the polymer chains in the composite.

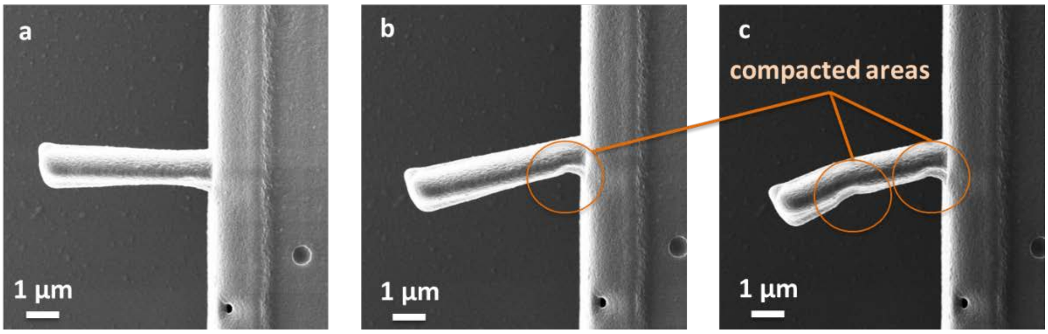

Figure 3.1 Helium ion induced bending of MPL-fabricated cantilevers

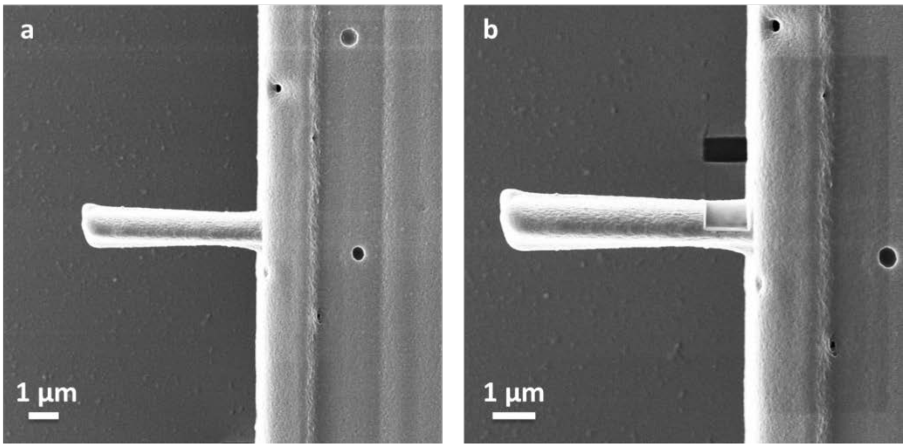

Figure 3.2 Gallium ion irradiated cantilever

To leverage the above bending effect for practical applications, we have performed mechanical modeling of the bending of the MPL-fabricated structures due to helium ion irradiation. For this, the cantilever bending presented in Figure 3.1 is used for proof of concept. To begin, the distribution of helium ions inside the irradiated volume of the material is estimated using the well-known Monte Carlo ion-sample interaction simulation tool SRIM (Ziegler et al., 2010). The simulated depth distribution for 25 keV helium ions incident on SZ2080 is presented in Figure 3.3. The atomic composition of SZ2080 was measured employing Energy Dispersive X-ray (EDX) spectroscopy. The measured composition is 43.8% carbon, 24.8% oxygen, 16.9% silicon and 14.5% zirconium and the density of SZ2080 is equal to 1.2 g/cm^3.

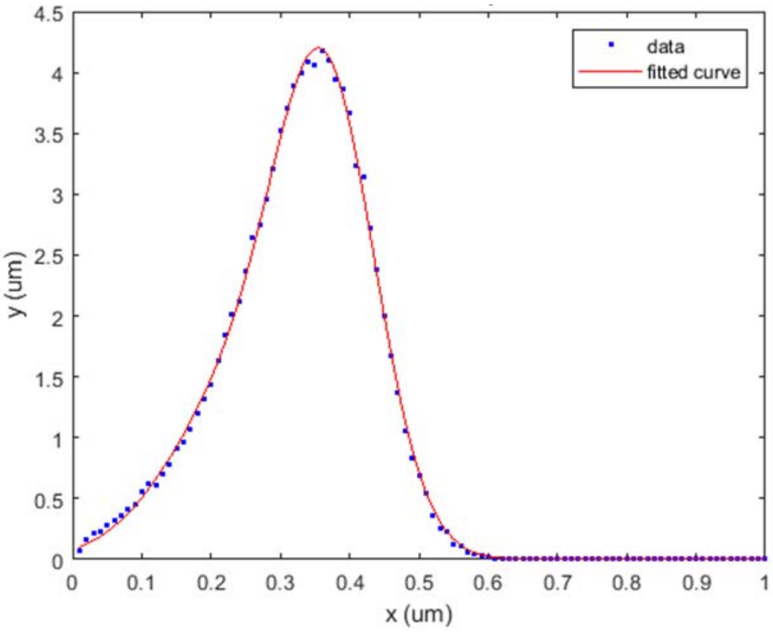

Figure 3.3 Helium ion distribution in depth calculated using SRIM.

The simulated ion distribution can be approximated by the superposition of two normal distributions. The result of the fitting process in MATLAB is:

$$y(x) = 3.30e^{-\left(\frac{x-0.37}{0.10}\right)^2} + 1.47e^{-\left(\frac{x-0.26}{0.15}\right)^2} \qquad (3.1)$$

The helium ions induce compressive residual stresses with a distribution proportional to the helium ion distribution. As a result, tensile residual stresses are created for the cantilever to equilibrate. At equilibrium, the system of equations below should be valid (Gere & Timošenko, 1997):

Equilibrium of forces
$$\int_A \sigma_{xx} dA = 0 \tag{3.2}$$

Equilibrium of moments in y-axis
$$\int_A z\sigma_{xx} dA = 0 \tag{3.3}$$

Equilibrium of moments in z-axis
$$\int_A y\sigma_{xx} dA = \frac{EI}{R} \tag{3.4}$$

where σ_{xx} are the axial stresses, E is the Young's Modulus, I is the second moment of area and R is the cantilever radius, measured from Figure 3.1(b) to be 0.15 μm. The x-axis is considered parallel to the cantilever, the z-axis coincides with the normal axis to the substrate and the y-axis arises if an orthonormal coordinate system is considered. In this way, the helium ion distribution can relate to the resulting bending of the cantilever and an analytical model connecting the irradiation with the resulting deformation can be created.

The goal of this endeavor is an analytical model that connects the irradiation area with the resulted deformation. The analytical model will be validated with a corresponding finite element analysis model. Analytical modeling would be nevertheless preferred as it offers inversion to enable computation of the irradiation area for achieving the desired deformation. Hence, helium-ion irradiation could be employed as a tool for correcting fabrication errors in applications with very narrow geometrical tolerances, such as micro-optics. These errors can be due to material shrinkage, and their prediction and compensation during design process is typically very tough.

4. Scalable Phononic Metamaterials: Inverse Design and Experimental Validation of Tunable Bandgaps

In this work, we provide an automated, systematic design approach for phononic metamaterial lattice structures with tailored, tunable wave propagation behavior at different length scales. We also fabricate these designed structures and experimentally characterize their wave propagation properties across different length scales.

Phononic metamaterials have garnered significant interest due to their ability to control and manipulate sound waves (Deymier, 2013; Liu et al., 2000). A key feature of phononic metamaterials is the existence of bandgaps, frequency ranges wherein wave propagation is prohibited in certain directions through the structure (Li et al., 2019; Sepehri et al., 2020). This characteristic makes them ideal for applications in sound insulation, vibration control, and acoustic waveguiding (Bacigalupo et al., 2019; Delsing et al., 2019; Dong et al., 2020).

Designing metamaterials with specific phononic bandgaps has significant implications across various fields. For sound insulation and noise reduction, materials with tailored bandgaps can be used to create barriers that block unwanted sound frequencies, improving acoustic environments in buildings, vehicles, and industrial settings. In vibration control, these materials can be employed to dampen vibrations in mechanical systems, enhancing the performance and longevity of machinery and structures (Chen et al., 2017). Additionally, phononic metamaterials are essential for developing advanced acoustic devices such as waveguides, filters, and resonators (Claeys et al., 2017). These devices are critical components in telecommunications, signal processing, and sensor technologies. The ability to design materials with precise bandgap properties opens up new possibilities for enhancing the performance of these devices (Li et al., 2017).

The design and fabrication of phononic metamaterials with specific bandgaps have been extensively researched. Traditional methods often involve trial-and-error approaches, which are time-consuming and inefficient. Early work focused on simple periodic structures, such as arrays of rods or holes, to create bandgaps (Kushwaha et al., 1993; Martínez-Sala et al., 1995). Researchers have also explored various materials, geometries, and configurations to achieve desired acoustic properties (Krushynska et al., 2018). Recent advances leverage computational methods to predict and optimize the bandgap properties of phononic metamaterials. Techniques such as finite element analysis (FEA) have been employed to simulate wave propagation and identify bandgaps in complex structures (Frenzel et al., 2013; Qureshi et al., 2016).

Building upon our previous work and expertise on inverse-designed metamaterials with tailored linear elastic mechanical behavior (Meier et al., 2024) and combining automated FEA simulations with Bayesian optimization methods (Sheikh et al., 2022), we developed an automated framework for the design of tunable phononic metamaterials at different length scales and for specific frequency ranges. We used COMSOL Multiphysics accessed through automated MATLAB scripts for FEA simulations to determine the bandgap diagrams of metamaterial unit cell designs. Our framework is demonstrated with the 3D unit cell shown in Figure 4.1, varying the three geometrical parameters: unit cell length (L), radius of spheres (R_s), and beam radius (R_b). These parameters formed the basis for our optimization process and to tailor the bandgap for certain frequency ranges. The unit cell design was chosen because it can be fabricated easily through different additive manufacturing techniques at various scales.

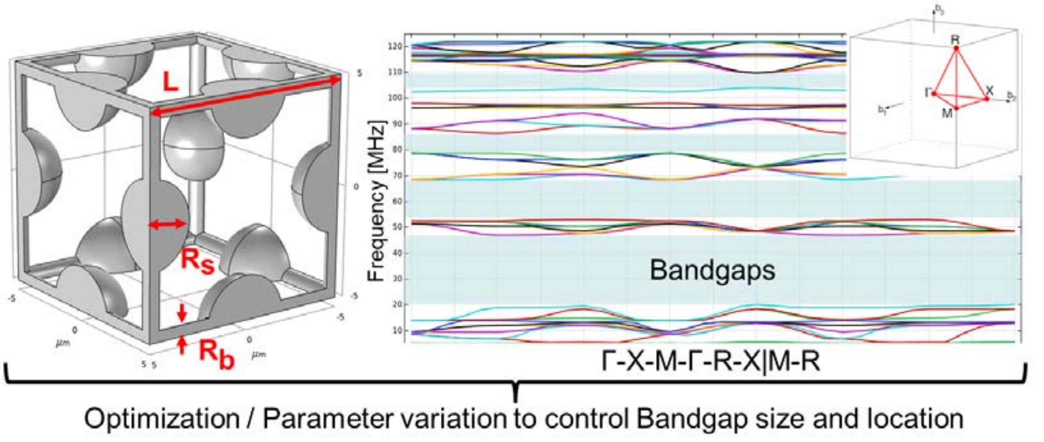

Figure 4.1 *3D model of a parametrized unit cell. The cubic symmetric unit cell features spherical masses connected by cylindrical beams. The parameters, including unit cell length (L), sphere radius (R_s), and beam radius (R_b), can be adjusted for optimization and to tune bandgap locations. The right side displays the calculated band structure for the 3D unit cell, clearly illustrating the presence of bandgaps.*

We conducted the optimization using a multi-objective Bayesian optimization framework, specifically applying Thompson Sampling Efficient Multi-Objective Optimization (TS-EMO) provided by Bradford et al. (Bradford et al., 2018) in the AutoOED interface developed by Tian et al. (Tian et al., 2021). This approach allowed us to inversely design the metamaterials, optimizing for specific bandgaps by efficiently exploring the parameter space. The optimization process seamlessly integrated with the FEA simulations, automating the iterative design and evaluation cycles. Users can easily define design parameter ranges, constraints, and cost functions for the optimization goals based on specific applications and requirements. Figure 4.2 shows how varying the geometrical parameters can be used to tailor the bandgap size in specific frequency ranges. With each simulation taking only a few minutes and the optimization converging in a few iterations, new, tailored bandgap metamaterials can be developed within hours. Moreover, the framework can easily be expanded to other unit cell designs and complex lattice structures depending on the user's requirements.

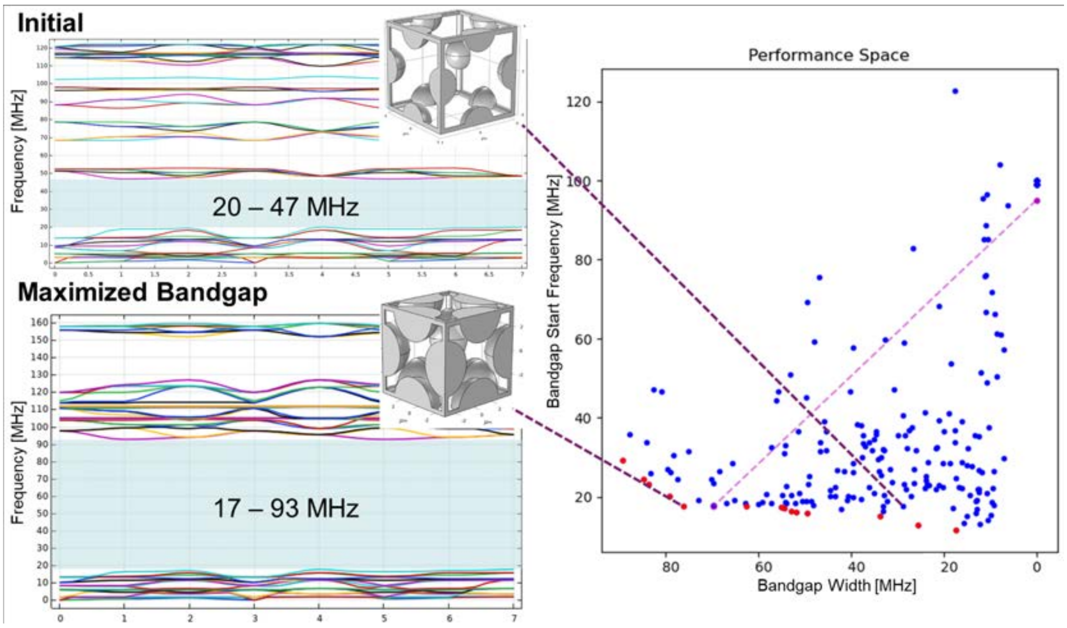

<u>Figure 4.2</u> Effect of parameter variation on tunable bandgaps. The left side compares the initial unit cell structure with the optimized unit cell designed for maximum bandgap width. By varying the design parameters, the width and location of bandgaps can be tuned. The right side illustrates the performance space of the optimization, highlighting the ability to tailor and select desired designs with specific tunable bandgap locations. This demonstrates the impact of parameter adjustments on the bandgap properties of the unit cell.

To validate theoretical simulation results, we fabricated selected optimized 5×5×5 periodic designs at two different scales with the same parameter ratios. At the macroscale, structures were fabricated using single-photon polymerization (1PP) (Anycubic Photon D2), with a unit cell length of 10 mm. For microscale fabrication, we employed two-photon polymerization (2PP), as described in previous chapters, creating unit cells at a length of 80 µm.

As shown by previous studies, varying the wavevector and directly measuring the band diagram of structures is challenging and requires sophisticated, precise equipment (Gorishnyy et al., 2005; Kai et al., 2023). According to most other studies (Groß et al., 2023; Krödel & Daraio, 2016), we opted to measure the transmission loss of the fabricated structures using laser vibrometry (Polytec GmbH, PSV-500 Scanning Vibrometer). Piezo transducers (Thorlabs, Inc., 150V co-fired square piezo stacks and APC International, piezo discs) were used to sweep through a range of frequencies, and the velocity magnitude of vibrations was recorded. The transmission loss ratio was calculated by comparing the FFT velocity magnitudes of the transducer alone and the transducer with the attached structure. This process was repeated for both macro and microscale structures to validate the bandgaps experimentally. In frequencies corresponding to a bandgap, the transmission loss was greater, validating decaying phononic waves inside the structure.

Figures 4.3 presents a comparison of theoretical and experimental results of the frequency sweep tests for the micro- and macroscale structures. At both scales, the structures showed significant drops in wave transmission within the bandgap frequencies, corroborating the simulation outcomes and band diagrams. The experimental validation results qualitatively match the theoretical predictions, with transmission loss significantly dropping in the regions of the predicted phononic bandgaps. Discrepancies between the experimental and theoretical results can be attributed to several factors, including manufacturing imperfections, material property variations, experimental setup limitations, and noise. Small defects or inconsistencies in the fabricated structures can affect wave propagation, leading to differences in the observed bandgap characteristics. Additionally, variations in the material properties, such as elasticity, from the idealized values used in simulations can also contribute to these deviations. Finally, inaccuracies in the experimental setup, such as alignment issues with the laser vibrometry or the piezo transducer, and noise components may introduce measurement errors, affecting the experimental transmission loss data.

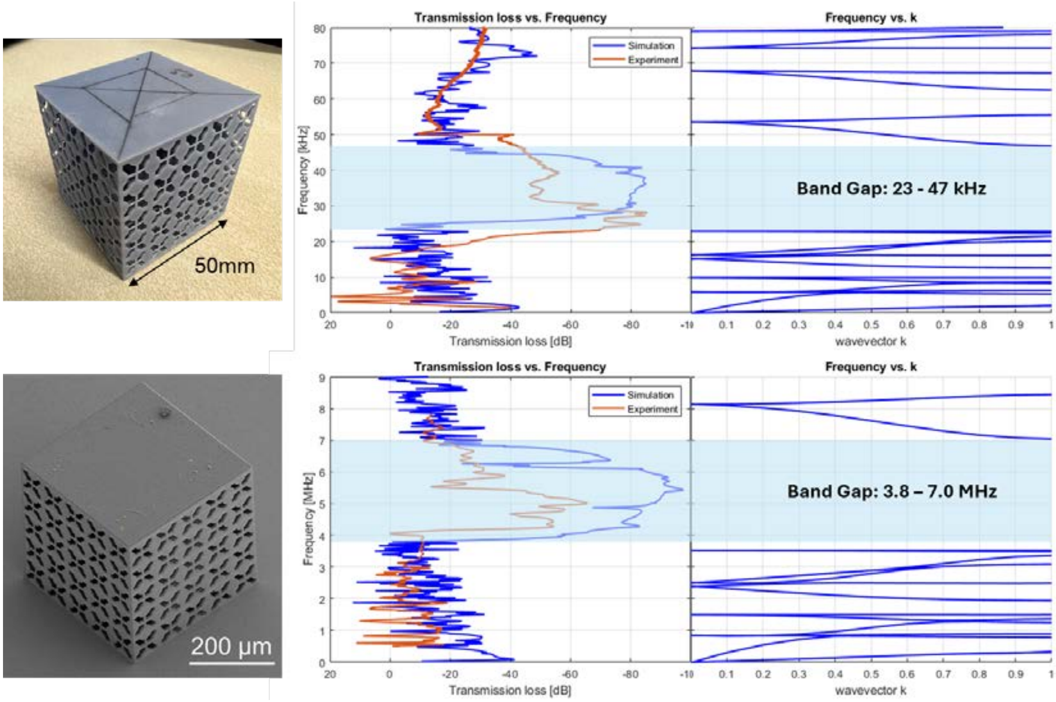

<u>Figure 4.3</u> Comparison of experimental and simulation results for scalable metamaterials with tuned bandgap properties. This figure demonstrates the scalability and consistency of the metamaterial design, with both macro-scale (50 mm) and micro-scale (400 µm) structures exhibiting tunable bandgap properties. Top Row: Results for the 50 mm 1PP metamaterials. Left: Photograph of the fabricated structure. Middle: Comparison of theoretical and experimental transmission loss data, showing good agreement. Right: Bandgap diagram highlighting strong transmission loss at frequencies of bandgaps. Bottom Row: Results for the 400 µm 2PP structure with the same parameter ratios as the 1PP structure. Left: SEM image of the 400 µm structure. Middle: Comparison of theoretical and experimental transmission loss data, showing good agreement. Right: Bandgap diagram highlighting strong transmission loss at bandgap frequencies.

Overall, the results from this study demonstrate the effectiveness of the automated design framework for creating metamaterials with tailored, scalable phononic bandgaps. Figure 4.3 shows that the experimental frequency sweep tests at both macro and microscale corroborate the theoretical predictions, with significant drops in wave transmission observed within the bandgap frequencies. This qualitative match between experimental and theoretical results underscores the potential of combining COMSOL FEA simulations with multi-objective Bayesian optimization to achieve precise control over phononic metamaterial properties. The multi-objective Bayesian optimization framework effectively navigated the complex parameter space, yielding optimal designs that met our objectives. Our findings demonstrated that the design approach is scalable and applicable to both macro and microscale. The successful fabrication and validation of structures at different scales underscore the versatility and robustness of the method.

The ability to design metamaterials with specific bandgaps has significant implications for various applications, including noise reduction, vibration control, and waveguiding. Despite observed deviations likely due to manufacturing imperfections, material property variations, and experimental setup limitations, the consistency of the results across different scales highlights the robustness of the design approach. Future work will focus on composite structures tailored for multiple bandgap regions and combining phononic properties with other mechanical properties such as stiffness, buckling behavior, and deformation mechanisms under load in a multi-objective optimization framework. The automated design and validation framework developed in this project can be adapted for other types of metamaterials and wave phenomena, potentially revolutionizing material design processes in multiple fields.

5. 3D Imaging of Micro-Architected Materials

The application of machine learning and automated routines for geometry generation and mechanical analysis are leading to the rapid exploration of the possible design spaces of mechanical metamaterials with tailored properties (Alderete et al., 2022; Ha et al., 2023; Sheikh et al., 2022; Vangelatos et al., 2021; Zeng et al., 2022). Coinciding with design advancements has been the development of mesoscale additive manufacturing techniques, enabling the production of arbitrarily shaped metamaterials with intricate nanoscale features and dimensions extending now up to several centimeters (Geng et al., 2019; Jonušauskas et al., 2019; Zheng et al., 2016). Among these, Two-photon polymerization (TPP) stands out for its fine and versatile printing capabilities, achieving sub-diffraction limit feature sizes at extremely high relative volumetric print rates.

As these developments proceed, new diagnostic tools and imaging techniques are becoming necessary to provide advanced *in-situ* diagnostics and to better quantify the detailed behavior and performance of these materials. In terms of imaging, existing methods like scanning electron microscopy (SEM) or helium ion microscopy (HIM) provide detailed surface images that can adequately resolve the nanoscale features of these materials (Surjadi et al., 2019). However, these imaging modalities fail to capture the internal deformation mechanics of these materials as they rely on the scattering of electrons or ions from the surface of complex structures which shield the interior members. Alternative techniques utilizing X-ray tomography have been developed that capture the interior deformation of these materials during mechanical compression, yet these techniques require specialized equipment paired to synchrotron radiation sources to achieve resolutions below 500 nm (Hu et al., 2021).

Addressing this diagnostic gap, we develop and demonstrate a technique for imaging polymeric metamaterials using various optically sectioned microscopy techniques such as confocal fluorescence microscopy, two-photon fluorescence (2P), three-photon fluorescence (3P), and third harmonic generation (THG) microscopy. We demonstrated that by adapting these techniques we can produce high-fidelity three-dimensional

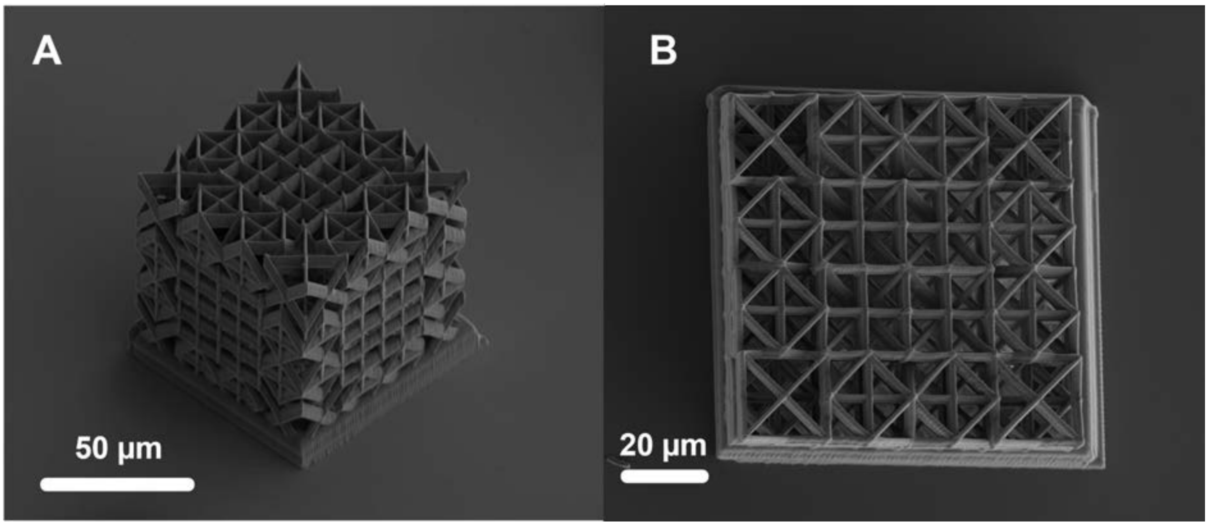

Figure 5.1 SEM Images of Exemplary TPP Structure (A) Orthogonal view of the lattice structure design that is fabricated with our two-photon polymerization setup. (B) Top view of the lattice shows internal beam members, but large sections of the view are masked by overlapping sections of the upper levels of the structure, making analysis of internal beam bending nearly impossible with these techniques.

renderings of these structures with near-diffraction-limited resolution and extract interesting information such as the formation of cracks across beam members – even deep inside of the lattice structures. Furthermore, we capture a series of three-dimensional images across discrete deformation steps to better understand the deformation mechanics of a prototypical metamaterial structure.

In our foundational work on this topic, published in Nano Letters (Blankenship et al., 2024), we present an exemplary 80 µm x 80 µm x 80 µm metamaterial structure depicted in Figure 5.1 that was printed on our two-photon polymerization setup. This structure contains lateral voxel dimensions ranging from 650 – 900 nm size and axial dimensions from 3.2 - 4 µm, which are reasonable feature sizes for high-throughput TPP prints. The refractive index of the polymerized resin material was measured to be approximately 1.48 at a wavelength of 488 nm. This agrees with similar measurements of the same polymer.(Žukauskas et al., 2015) Given that the refractive index mismatch of the polymer and surrounding air is large, and that the lattice has a complex spatial variation in refractive index, scattering becomes dominant after imaging only a few layers into the structure, limiting the achievable imaging depth. To overcome this, we envelop the structures in a droplet of mineral oil whose refractive index was determined to match that of the photopolymerized resin to mitigate scattering from the structure, thus significantly reducing scattering and enhancing imaging depth.

In this early investigation we utilize a 60X oil immersion objective with a 1.25 numerical aperture to capture the features of our lattice structures. These images yield lateral dimensions of roughly 1 – 1.3 µm and axial dimensions of 3.8 – 4.5 µm which is larger than the dimensions measured by the SEM. Subsequently cross-sectional images of the structure are imaged at 100 nm increments to generate a stack of images for three-dimensional reconstruction. Select and distinct confocal microscope images of the fabricated structure are directly compared to 800 nm thick slices of their solid model counterparts in Figure 5.2 which demonstrate the ability of this technique to adequately capture the internal features of the structure at various depths. Furthermore, we develop an

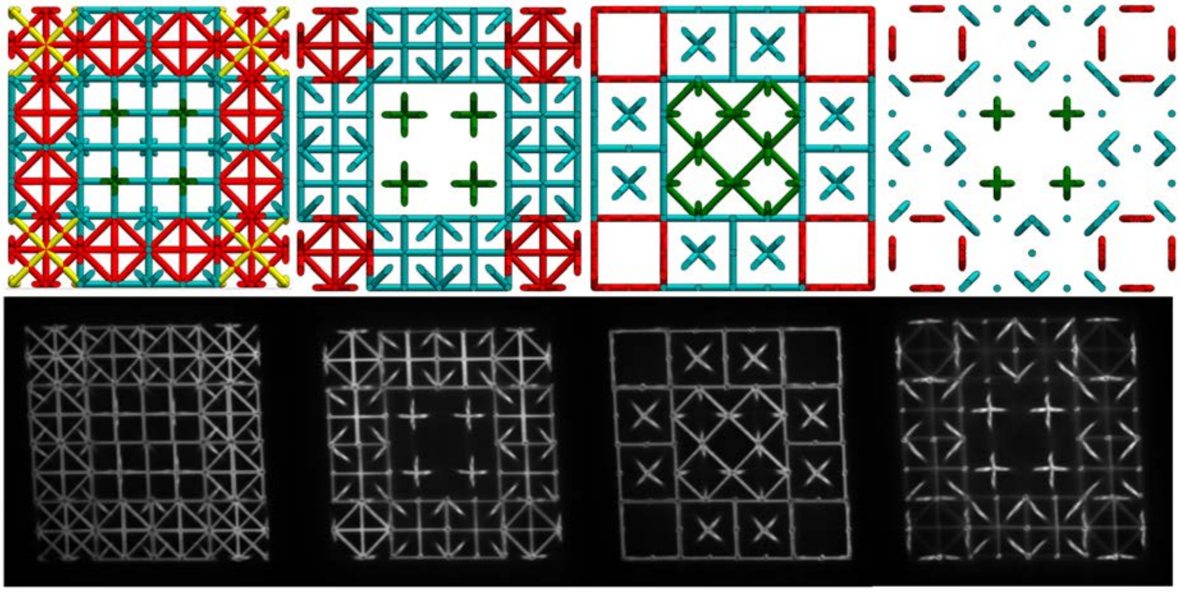

Figure 5.2 Confocal Images (Top) CAD renderings of 800 nm thick slices of the 4 x 4 x 4 lattice structure. (Bottom) Corresponding confocal images showing remarkable resemblance to the ideal shape.

open-source code that binarizes the outputs of the individual confocal images to generate a point cloud to represent the structure, and then subsequently generate a standard three-dimensional output file (.obj) of the structure.

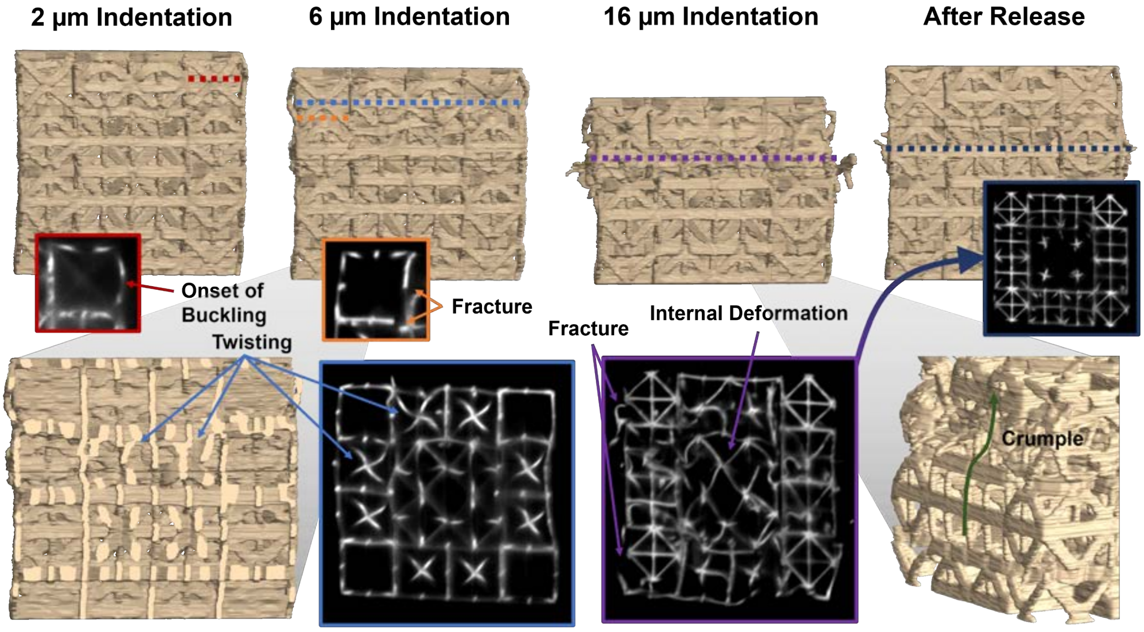

Figure 5.3 In-Situ Compression Testing (Top) 3D renderings at various indentation steps from 2 µm (left) to 16 µm (middle right) and after releasing the indentation tip (right). Various mechanical deformations across the different loading conditions are highlighted such as the onset of buckling, and the presence of fractures and plastic strain. (Bottom) (Left) vertical cross-sectional view of the rendering depicting the beams twisting at 6 µm of compression. This same phenomenon is captured in a correspond confocal slice (middle left, blue). At higher strains, sections of the metamaterial appear to crumple, which can be observed via imaging the internal structure (middle right) and investigating the exterior deformation of the structure (right).

As a demonstration, we perform a mechanical compression test on the structure at various steps between 0 and 16 µm. We first construct a specialized *in-situ* confocal micro compression apparatus shown in Figure 5.3 to incrementally compress structures and image between increments. Our methodology involves successively imaging entire z-stacks that encompass the volume of the metamaterial structure before incrementally moving the indenter in 2 µm steps. We should note that the incremental nature of the compression protocol does not generate a standard rate-controlled compression loading profile and thus measures periods of relaxation during imaging wherein the structure is held at static intervals of loading.

We have further planned to capture real-time 3D times of the structures during mechanical compression using a state of the art, ultra-high speed 5000 fps multiphoton microscope used for neuroimaging studies. We have teamed up with one of the world's leading multi-photon imaging experts, Na Ji, to begin studies on multi-photon imaging of metamaterials. In these early experiments we have identified promising avenues to image deep into TPP structures using 2P and 3P fluorescence microscopy, and image the formation of cracks during compression using THG microscopy. Although unpublished, we show simultaneously acquired 3P and THG images that show enhanced signal contrast at fracture sites.

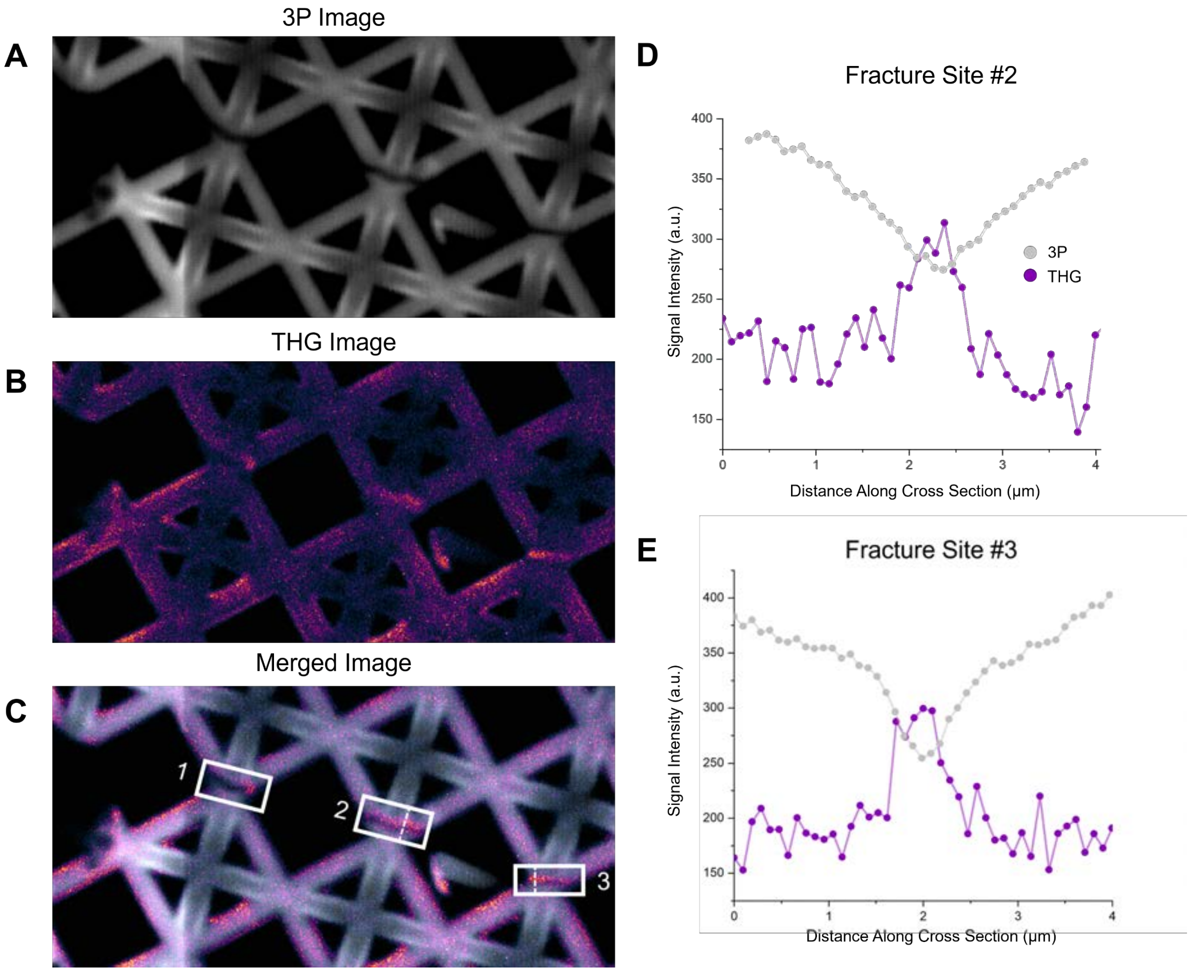

Figure 5.4 3P and THG Images of Fracture Beam Members (A) 3P image of a cross section with three cracked beam members (B) compared to the corresponding THG image measured at the slice position (C) The merged image shows that THG contrast aligns with the location of cracks (D) 3P and THG signal intensity measured across the highlighted cross sections for fracture site #2 and (E) fracture site #3, where THG signal increases at these locations and THG signal decreases.

In our ongoing work, we will extend these techniques to a 5000 frame per second multiphoton imaging setup, where we expect to capture load curves in tandem with 3D volumetric imaging to capture crack initiation and propagation events. There is also the possibility that we work to incorporate cells into the lattice structures to understand the deformation of cellular scaffolding to understand how different biological systems respond to imposed and self-induced stresses in their environments.

Overall, this work had yielded two publications, and will yield at least two more publications in the coming year.

6. Quantum Sensing Inside Micro-Architected materials

NV$^-$ centers exhibit exceptional photostability, spin-state selective fluorescence emission, and long spin coherence times at room temperature, which enable diverse applications under ambient conditions.(Castelletto & Boretti, 2020; Doherty et al., 2013; Kennedy et al., 2003; Stern et al., 2022) Of particular interest is leveraging the NV$^-$ center's sensitivity to local electromagnetic fields (Block et al., 2021; Dolde et al., 2011; Hong et al., 2013; Horowitz et al., 2012; Hruby et al., 2022; Weggler et al., 2020), strain (Knauer et al., 2020), and temperature (Andrich et al., 2018; Toyli et al., 2013) as a modality for micro and nanoscale metrology. However, most quantum sensing applications of NV-diamond have remained limited to diamond single crystal slabs, grown under pristine conditions and with specific lattice engineering and/or surface treatments to protect the coherence properties of the NV center. While these slabs demonstrate impressive sensitivity, experimental setups must be finely engineered around the slab; in particular, the short range (< 10nm) of NV-based sensing requires that analytes be brought into contact with the diamond crystal surface. Moreover, the high cost and mm-scale extent of these slabs severely limits applications having larger spatial areas of interest (Barry et al., 2016; Steinert et al., 2010).

Diamond nanoparticles (nanodiamonds, or NDs) hosting NV centers are an alternative platform for quantum sensing (Mochalin et al., 2012). Their advantages include extremely low costs and easy surface functionalization with a wide variety of moieties, enabling control of ND surface charge, colloidal stability, and direct targeting to regions of interest (Pan et al., 2023; Wu & Weil, 2022). NDs therefore offer exciting possibilities for both “deployable” quantum sensors and for sensing over broad areas using an ensemble of NDs, in both cases interrogating magnetic fields noninvasively with submicron-scale resolution and fully in three dimensions (3D).

We argue that advanced manufacturing techniques, including two-photon polymerization (TPP), provide a simple and compelling complement to the rich features of ND quantum sensors. Previously, in our manuscript entitled, “Complex Three-Dimensional Microscale Structures for Quantum Sensing Applications,” we have demonstrated the ability to incorporate nanodiamonds into TPP structures and measure temperature and magnetic field with high sensitivity (Blankenship et al., 2023). We outlined two key areas of improvement to enhance these sensors: first by being able to selectively pattern of nanodiamonds onto the surface of TPP structures, and secondly by extending the measurements to 3D volumes.

To address this first point, we developed a means to selectively pattern dense films of nanodiamonds onto a substrate using a technique called “bubble printing” in our work, entitled, “Spatially Resolved Quantum Sensing with High-Density Bubble-Printed Nanodiamonds”, published in Nano Letters. We write arbitrary patterns of nanodiamonds encompassing many lengths scales and use a specialized widefield lock-in imaging technique to capture 2D images of microwave resonances in the nanodiamonds from which temperature information can be extracted. This basic process is described in Figure 6.1. This study was exciting in the sense that it could then be used to construct analogous 3D patterning and imaging methods.

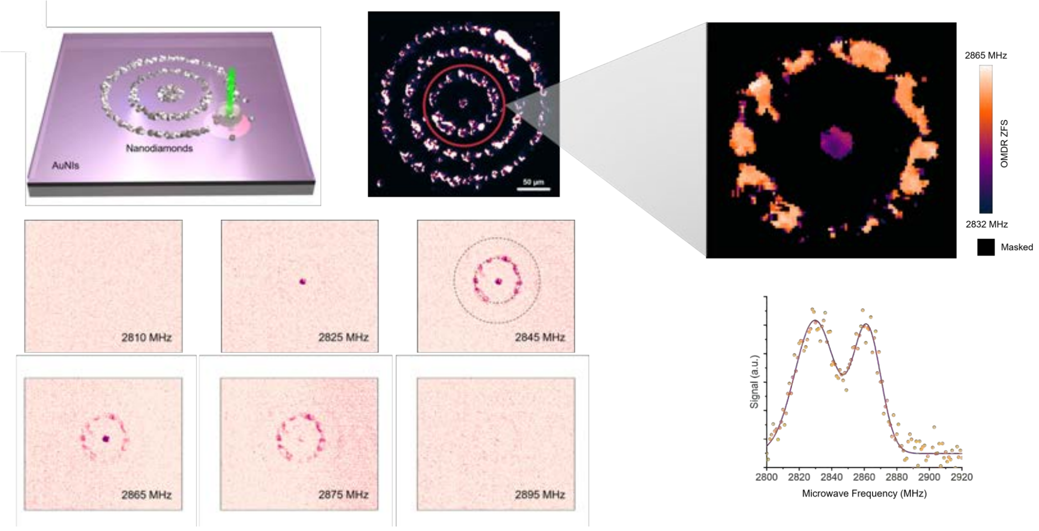

<u>Figure X5</u> Bubble Printing of Nanodiamonds for 2D Quantum Sensing (Top Left) Diagram depicting the bubble printing process (Top Middle) Nanodiamond tracks printed into concentric circles. (Bottom Left Images) Widefield lock-in ODMR images taken at 2810 MHz, 2825 MHz, 2845 MHz, 2865 MHz, 2875 MHz and 2895 MHz. (Top Right) These lock-in images were used to measure the ZFS (Bottom Right) Which can then be used to construct ODMR spectra that can be used to measure the local temperature at each pixel.

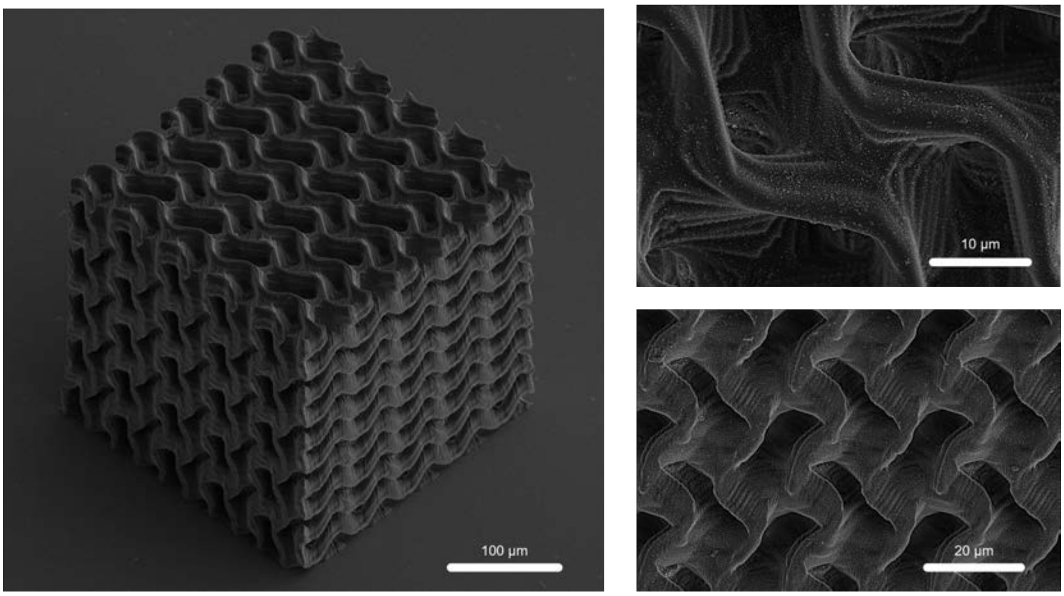

<u>Figure 6.2</u> SEM Images of Gyroid Structures (Left) Orthogonal view of structures with nanodiamond coating (Right) closeups of the surface of the structure where nanodiamonds are more clearly seen to coat the exterior surface.

Further extending these techniques we developed a means to fabricate large-scale TPP structures and uniformly coat them with nanodiamonds. Figure 6.2 shows a 150 µm x 150 µm x 150 µm porous gyroid structure onto which we scaffolded millions of nanodiamonds. Zoomed in images better depict the nanodiamond coatings.

Using similar image methods as described before, we construct 3D renderings of the gyroid structure, only that we spectrally isolate the nanodiamond fluorescence from the resin fluorescence by incorporating a spectral detection unit into the pathway of the confocal microscope. These renderings seen in Figure 6.3 show that we can image the entirety of the nanodiamond structure with high resolution.

We have also extracted ODMR spectra from individual confocal slices, using a modified variant of our lock-in detection schemes that is adapted to the way that confocal microscopes scan an image. We are working towards creating large scale ODMR maps encompassing hundreds of thousands of points across the location of the nanodiamonds in the structure to realize powerful new applications.

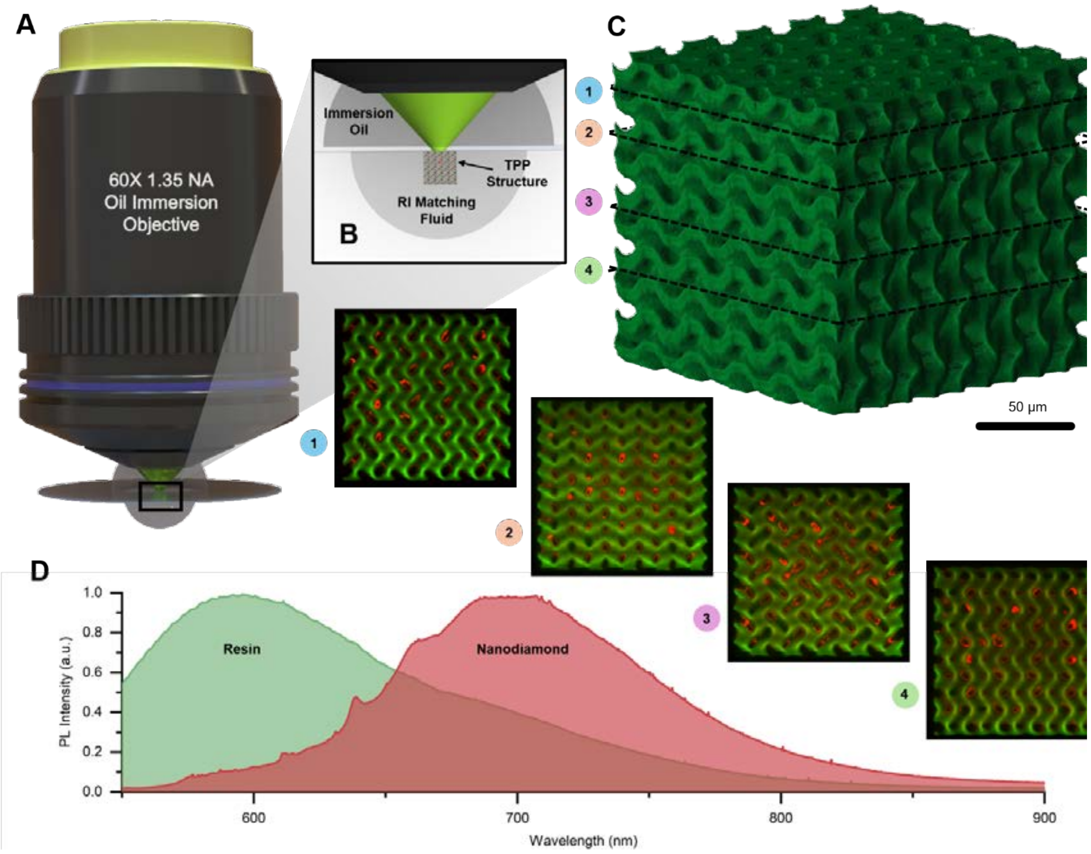

Figure 6.3 Dual color gyroid structure imaging: (A) Gyroid structures are imaged similarly to the methodology used in chapter 4.1, where (B) the structure of interest is enveloped in a refractive index matching fluid. (C) The structure can be optically reconstructed from many individual confocal slices, who can be spectrally separated to show the location of diamonds across the interior of the structure. This separation is determined based on the PL spectrum of the constituent components.

The development of structures that facilitate *in-situ* detection of chemical constituents at nanomolar concentrations. This effort aims to address an unmet need in electrochemistry for precise ionic sensing, particularly where *in-operando* measurements of ionic flow are challenging. Current methods, such as surface-enhanced infrared (SEIRAS) or Raman spectroscopy (SERS), rely on specific catalysts like Au, Ag, and Pd to provide sufficient surface enhancement, imposing restrictive limitations. *Ex-situ* approaches, such as mass spectrometry, also pose significant challenges for time-resolved measurements. The creation of 3D quantum sensors capable of overcoming these limitations represents a significant advancement in the field.

The integration of nanodiamond (ND) particles within scaffold walls to serve as three-dimensional multimodal sensors is an obvious application space. These sensors are designed to detect and identify analyte molecules flowing through the structures, as well as to monitor the surrounding temperature of the fluid. This dual functionality significantly broadens the scope of diagnostics available in microscale fluidic environments, enabling the characterization of reactions in flow and the dynamics of fluids within porous structures. Demonstrative experiments could, for instance, measure the concentration of paramagnetic ions, such as Gd3+, through porous ND-filled scaffolds, with a target sensitivity of 1 μM.

Another potential application would be to utilize ND quantum sensors for *in-situ* monitoring of critical heterogeneous catalytic reactions and diffusion processes within microscale 3D chambers, or "microreactors." Current techniques, including magnetic resonance imaging (MRI) with hyperpolarized materials, are limited by their spatial resolution. By embedding nanodiamond sensors into the walls of 3D porous structures, a platform will be developed for detailed study of heat and mass transport phenomena, reaction kinetics, and catalyst dynamics at unprecedented spatial resolutions. This approach aims to enhance *in-situ* probes of reactor conditions, which are crucial for process optimization.

C. Work in the Subsequent Funding Period

During the next and final year of the project, our research will include work on ongoing projects, effectively combining their outcomes to form an integrated design, manufacturing and characterization platform. Firstly, a large portion of our research effort will be spent on the ongoing project of biomimetic structures. To advance this work, we will complete and fully utilize the fast galvanometric setup that is capable of printing structures in the several mm scale at high speeds. A computational model of nacre-inspired plates will be developed in the simulation environment of LS-Dyna. A material model of self-assembled peptide fibrils will be developed and employed. The selection of the appropriate model and the determination of the corresponding parameters will be based on experimental data collected using our custom mechanical testing device. The development and validation of the material model will be based on an iterative feedback simulation, like the process followed during the development and validation of the material model used in the design of hinges inspired by the diabolical ironclad beetle. Subsequently, the developed material model will be integrated into a simulation model. More specifically, an appropriate CAD model, such as the model that was used for the fabrication of nacre-inspired plates, will be imported in LS-Dyna and discretized using appropriate finite elements. In addition, two different material models will be employed: the first one for the MPL-fabricated structure and the second one for the peptide fibrils. Moreover, the contact interfaces between the MPL-fabricated structure and the fibrils should be modeled. LS-Dyna offers the capability to employ different contact models, each one appropriate for simulating interfaces of different types. It should be noted that the employed contact model should contribute to the higher convergence between the simulation and the experiments, should be compatible with the employed type of finite elements and the used material models, and should not dramatically increase the computational time. At this point, development and validation of a complex mechanical digital twin of a nacre-inspired structure required many iterations and will be partially based on a trial-and-error process.

Secondly, an LS-Dyna model can be integrated into an optimization process employing LS-OPT. In more detail, LS-OPT is a multi-objective optimization framework that uses LS-Dyna for solution evaluation (Goel & Stander, 2007). Moreover, it offers the capability to employ different optimization algorithms, such as the well-known genetic algorithm NSGA-II, or optimization techniques, or create a Pareto solution set. Hence, an optimized nacre-like structure can be designed using the above mechanical model. Consequently, the required number of experiments can be significantly decreased, and an optimal structure can be provided in a shorter time while spending much reduced laboratory resources.

Beyond these, LS-Dyna can be integrated into a topology optimization process using LS-TaSC, developed by Livermore Software Technology Corporation, the developer of LS-Dyna and LS-OPT. More specifically, topology optimization is a mathematical technique that optimizes material layout inside a particular design space for a given combination of loads, boundary conditions, and constrains to maximize system performance (Sigmund & Maute, 2013). LS-TaSC is specially developed for crashworthiness applications where the most important design criterion is the internal energy absorption and the energy density distribution should be uniform in the optimized structure (Roux, 2016). For that reason, the algorithm removes unwanted material from specific areas of the structure without decreasing its mechanical performance, which is evaluated using LS-Dyna. Our plans include work on a bio-inspired case-study structure like cuttlebone. Cuttlebone is a natural lattice structure that has attracted the interest of the research community thanks to its superior stiffness and specific energy absorption (Mao et al., 2021). The combination of topology optimization and biomimicry in the case of cuttlebone has already been demonstrated, but employing metallic materials and using millimeter-size unit cells. However, our work will focus on the design of millimeter-sized structures with micrometric unit cells employing Multiphoton Lithography for fabrication purposes. We therefore anticipate achieving structures with even higher mechanical properties thanks to the ultra-high fabrication resolution (Meier et al., 2024).

Finally, we are planning to apply Digital Image Correlation (DIC) at MPL-fabricated structures. According to the International Digital Image Correlation Society, "DIC is an optically-based technique used to measure the evolving full-field 2D or 3D coordinates on the surface of a test piece throughout a mechanical test" (International Digital Image Correlation Society et al., 2018). In that way, displacements can be measured and the strain, and the corresponding stress, field can be computed, which is crucial for mechanical design and evaluation of finite element analysis simulations. Beyond these, a generalization of DIC is Digital Volumetric Correlation (DVC), based on which the full-field three-dimensional deformations are calculated (Bay et al., 1999; Huang et al., 2011). The main difference between DIC and DVC is that in DIC only deformations in the surface can be calculated. In contrast, in DVC the deformations in the whole volume of the specimen can be calculated. Images used in DVC can be obtained employing confocal microscopy, X-ray computed tomography, etc. However, the implementation of DVC using a volumetric image dataset obtained using confocal microscopy could be challenging because confocal microscopy is an incremental imaging process. In more detail, in confocal microscopy, the specimen is scanned in order for the fluorophores to be active and an image to be incrementally obtained. In the case of continuous deformation of the specimen, this means that the obtained image is not a snapshot of incremental deformation of the specimen but stitching of different snapshots. In other words, a point of the specimen continues to be displaced until the whole section of the specimen is scanned, but no information about the displacement of this point is provided until this point is scanned again. This disadvantage can be critical in the case of the application of high strains when the material displacement speed can be comparable with the scanning speed. On the other hand, the employment of X-rays for imaging purposes can cause significant changes in the material composition or destroy the specimen. A very promising imaging technique could be Light Sheet Fluorescence Microscopy (LSFM) (Stelzer et al., 2021). More specifically, in LSFM, the sample is illuminated by a laser beam which is focused only in one direction creating a light sheet. Hence, a section of the sample is illuminated and its fluorescence is detected from a camera which is vertically located to the light sheet. In that way, a snapshot of the section is obtained and the photodamage is minimized.

References

Adler-Abramovich, L., Arnon, Z. A., Sui, X., Azuri, I., Cohen, H., Hod, O., Kronik, L., Shimon, L. J. W., Wagner, H. D., & Gazit, E. (2018). Bioinspired Flexible and Tough Layered Peptide Crystals. Advanced Materials, 30(5), 1704551. https://doi.org/10.1002/adma.201704551

Alderete, N. A., Pathak, N., & Espinosa, H. D. (2022). Machine learning assisted design of shape-programmable 3D kirigami metamaterials. Npj Computational Materials, 8(1), Article 1. https://doi.org/10.1038/s41524-022-00873-w

Allen, F. I. (2021). A review of defect engineering, ion implantation, and nanofabrication using the helium ion microscope. Beilstein Journal of Nanotechnology, 12, 633–664. https://doi.org/10.3762/bjnano.12.52

Andrich, P., Li, J., Liu, X., Heremans, F. J., Nealey, P. F., & Awschalom, D. D. (2018). Microscale-Resolution Thermal Mapping Using a Flexible Platform of Patterned Quantum Sensors. Nano Letters, 18(8), 4684–4690. https://doi.org/10.1021/acs.nanolett.8b00895

Bacigalupo, A., Lepidi, M., Gnecco, G., Vadalà, F., & Gambarotta, L. (2019). Optimal Design of the Band Structure for Beam Lattice Metamaterials. Frontiers in Materials, 6, 2. https://doi.org/10.3389/fmats.2019.00002

Bal, B., Karaveli, K. K., Cetin, B., & Gumus, B. (2019). The Precise Determination of the Johnson–Cook Material and Damage Model Parameters and Mechanical Properties of an Aluminum 7068-T651 Alloy. Journal of Engineering Materials and Technology, 141(4), 041001. https://doi.org/10.1115/1.4042870

Barauskas, R., & Abraitienė, A. (2007). Computational analysis of impact of a bullet against the multilayer fabrics in LS-DYNA. International Journal of Impact Engineering, 34(7), 1286–1305. https://doi.org/10.1016/j.ijimpeng.2006.06.002

Barry, J. F., Turner, M. J., Schloss, J. M., Glenn, D. R., Song, Y., Lukin, M. D., Park, H., & Walsworth, R. L. (2016). Optical magnetic detection of single-neuron action potentials using quantum defects in diamond. Proceedings of the National Academy of Sciences, 113(49), 14133–14138. https://doi.org/10.1073/pnas.1601513113

Bay, B. K., Smith, T. S., Fyhrie, D. P., & Saad, M. (1999). Digital volume correlation: Three-dimensional strain mapping using X-ray tomography. Experimental Mechanics, 39(3), 217–226. https://doi.org/10.1007/BF02323555

Blankenship, B. W., Jones, Z., Zhao, N., Singh, H., Sarkar, A., Li, R., Suh, E., Chen, A., Grigoropoulos, C. P., & Ajoy, A. (2023). Complex Three-Dimensional Microscale Structures for Quantum Sensing Applications. Nano Letters, 23(20), 9272–9279. https://doi.org/10.1021/acs.nanolett.3c02251

Blankenship, B. W., Meier, T., Zhao, N., Mavrikos, S., Arvin, S., De La Torre, N., Hsu, B., Seymour, N., & Grigoropoulos, C. P. (2024). Three-Dimensional Optical

Imaging of Internal Deformations in Polymeric Microscale Mechanical Metamaterials. Nano Letters. https://doi.org/10.1021/acs.nanolett.3c04421

Block, M., Kobrin, B., Jarmola, A., Hsieh, S., Zu, C., Figueroa, N. L., Acosta, V. M., Minguzzi, J., Maze, J. R., Budker, D., & Yao, N. Y. (2021). Optically Enhanced Electric Field Sensing Using Nitrogen-Vacancy Ensembles. Physical Review Applied, 16(2), 024024. https://doi.org/10.1103/PhysRevApplied.16.024024

Bradford, E., Schweidtmann, A. M., & Lapkin, A. (2018). Efficient multiobjective optimization employing Gaussian processes, spectral sampling and a genetic algorithm. Journal of Global Optimization, 71(2), 407–438. https://doi.org/10.1007/s10898-018-0609-2

Cai, X., Xu, W., Ren, C., Zhang, L., Zhang, C., Liu, J., & Yang, C. (2024). Recent progress in quantitative analysis of self-assembled peptides. Exploration, 4(4), 20230064. https://doi.org/10.1002/EXP.20230064

Castelletto, S., & Boretti, A. (2020). Silicon carbide color centers for quantum applications. Journal of Physics: Photonics, 2(2), 022001. https://doi.org/10.1088/2515-7647/ab77a2

Chen, W.-F., & Han, D. J. (2007). Plasticity for structural engineers. J. Ross Pub.

Chen, Y., Li, T., Scarpa, F., & Wang, L. (2017). Lattice Metamaterials with Mechanically Tunable Poisson's Ratio for Vibration Control. Physical Review Applied, 7(2), 024012. https://doi.org/10.1103/PhysRevApplied.7.024012

Claeys, C., Rocha De Melo Filho, N. G., Van Belle, L., Deckers, E., & Desmet, W. (2017). Design and validation of metamaterials for multiple structural stop bands in waveguides. Extreme Mechanics Letters, 12, 7–22. https://doi.org/10.1016/j.eml.2016.08.005

Cowper, G. R., & Symonds, P. S. (1957). Strain-hardening and Strain-rate Effects in the Impact Loading of Cantilever Beams. In Technical Report. Division of Applied Mathematics, Brown University.

Delsing, P., Cleland, A. N., Schuetz, M. J. A., Knörzer, J., Giedke, G., Cirac, J. I., Srinivasan, K., Wu, M., Balram, K. C., Bäuerle, C., Meunier, T., Ford, C. J. B., Santos, P. V., Cerda-Méndez, E., Wang, H., Krenner, H. J., Nysten, E. D. S., Weiß, M., Nash, G. R., … Westerhausen, C. (2019). The 2019 surface acoustic waves roadmap. Journal of Physics D: Applied Physics, 52(35), 353001. https://doi.org/10.1088/1361-6463/ab1b04

Deymier, P. A. (Ed.). (2013). Acoustic Metamaterials and Phononic Crystals (Vol. 173). Springer Berlin Heidelberg. https://doi.org/10.1007/978-3-642-31232-8

Doherty, M. W., Manson, N. B., Delaney, P., Jelezko, F., Wrachtrup, J., & Hollenberg, L. C. L. (2013). The nitrogen-vacancy colour centre in diamond. Physics Reports, 528(1), 1–45. https://doi.org/10.1016/j.physrep.2013.02.001

Dolde, F., Fedder, H., Doherty, M. W., Nöbauer, T., Rempp, F., Balasubramanian, G., Wolf, T., Reinhard, F., Hollenberg, L. C. L., Jelezko, F., & Wrachtrup, J. (2011).

Sensing electric fields using single diamond spins. Nature Physics, 7(6), 459–463. https://doi.org/10.1038/nphys1969

Dong, H.-W., Zhao, S.-D., Wang, Y.-S., Cheng, L., & Zhang, C. (2020). Robust 2D/3D multi-polar acoustic metamaterials with broadband double negativity. Journal of the Mechanics and Physics of Solids, 137, 103889. https://doi.org/10.1016/j.jmps.2020.103889

El-Tamer, A., Hinze, U., & Chichkov, B. N. (2021). Two-Photon Polymerization in Optics, Microfluidics, and Biomedicine. In K. Sugioka (Ed.), Handbook of Laser Micro- and Nano-Engineering (pp. 1691–1735). Springer International Publishing. https://doi.org/10.1007/978-3-030-63647-0_35

Frenzel, T., David Brehm, J., Bückmann, T., Schittny, R., Kadic, M., & Wegener, M. (2013). Three-dimensional labyrinthine acoustic metamaterials. Applied Physics Letters, 103(6), 061907. https://doi.org/10.1063/1.4817934

Geng, Q., Wang, D., Chen, P., & Chen, S.-C. (2019). Ultrafast multi-focus 3-D nano-fabrication based on two-photon polymerization. Nature Communications, 10(1), 2179. https://doi.org/10.1038/s41467-019-10249-2

Gere, J. M., & Timošenko, S. P. (1997). Mechanics of materials (4. ed). PWS Publ.

Goel, T., & Stander, N. (2007). Multi-Objective Optimization Using LS-OPT. . . LS.

Gonzalez-Hernandez, D., Varapnickas, S., Bertoncini, A., Liberale, C., & Malinauskas, M. (2023). Micro-Optics 3D Printed via Multi-Photon Laser Lithography. Advanced Optical Materials, 11(1), 2201701. https://doi.org/10.1002/adom.202201701

Gorishnyy, T., Ullal, C. K., Maldovan, M., Fytas, G., & Thomas, E. L. (2005). Hypersonic Phononic Crystals. Physical Review Letters, 94(11), 115501. https://doi.org/10.1103/PhysRevLett.94.115501

Groß, M. F., Schneider, J. L. G., Wei, Y., Chen, Y., Kalt, S., Kadic, M., Liu, X., Hu, G., & Wegener, M. (2023). Tetramode Metamaterials as Phonon Polarizers. Advanced Materials, 35(18), 2211801. https://doi.org/10.1002/adma.202211801

Ha, C. S., Yao, D., Xu, Z., Liu, C., Liu, H., Elkins, D., Kile, M., Deshpande, V., Kong, Z., Bauchy, M., & Zheng, X. (Rayne). (2023). Rapid inverse design of metamaterials based on prescribed mechanical behavior through machine learning. Nature Communications, 14(1), Article 1. https://doi.org/10.1038/s41467-023-40854-1

Hong, S., Grinolds, M. S., Pham, L. M., Le Sage, D., Luan, L., Walsworth, R. L., & Yacoby, A. (2013). Nanoscale magnetometry with NV centers in diamond. MRS Bulletin, 38(2), 155–161. https://doi.org/10.1557/mrs.2013.23

Horowitz, V. R., Alemán, B. J., Christle, D. J., Cleland, A. N., & Awschalom, D. D. (2012). Electron spin resonance of nitrogen-vacancy centers in optically trapped nanodiamonds. Proceedings of the National Academy of Sciences, 109(34), 13493–13497. https://doi.org/10.1073/pnas.1211311109

Hruby, J., Gulka, M., Mongillo, M., Radu, I. P., Petrov, M. V., Bourgeois, E., & Nesladek, M. (2022). Magnetic field sensitivity of the photoelectrically read nitrogen-vacancy centers in diamond. Applied Physics Letters, 120(16), 162402. https://doi.org/10.1063/5.0079667

Hu, W., Cao, X., Zhang, X., Huang, Z., Chen, Z., Wu, W., Xi, L., Li, Y., & Fang, D. (2021). Deformation mechanisms and mechanical performances of architected mechanical metamaterials with gyroid topologies: Synchrotron X-ray radiation in-situ compression experiments and 3D image based finite element analysis. Extreme Mechanics Letters, 44, 101229. https://doi.org/10.1016/j.eml.2021.101229

Huang, J., Pan, X., Li, S., Peng, X., Xiong, C., & Fang, J. (2011). A DIGITAL VOLUME CORRELATION TECHNIQUE FOR 3-D DEFORMATION MEASUREMENTS OF SOFT GELS. International Journal of Applied Mechanics, 03(02), 335–354. https://doi.org/10.1142/S1758825111001019

Hutchins, D. A. (1988). Ultrasonic Generation by Pulsed Lasers. In Physical Acoustics (Elsevier, pp. 21–123).

International Digital Image Correlation Society, Jones, E., Iadicola, M., Bigger, R., Blaysat, B., Boo, C., Grewer, M., Hu, J., Jones, A., Klein, M., Raghavan, K., Reu, P., Schmidt, T., Siebert, T., Simenson, M., Turner, D., Vieira, A., & Weikert, T. (2018). A Good Practices Guide for Digital Image Correlation (1st ed.). International Digital Image Correlation Society. https://doi.org/10.32720/idics/gpg.ed1

Jonušauskas, L., Gailevičius, D., Rekštytė, S., Baldacchini, T., Juodkazis, S., & Malinauskas, M. (2019). Mesoscale laser 3D printing. Optics Express, 27(11), 15205–15221. https://doi.org/10.1364/OE.27.015205

Kai, Y., Dhulipala, S., Sun, R., Lem, J., DeLima, W., Pezeril, T., & Portela, C. M. (2023). Dynamic diagnosis of metamaterials through laser-induced vibrational signatures. Nature, 623(7987), 514–521. https://doi.org/10.1038/s41586-023-06652-x

Kennedy, T. A., Colton, J. S., Butler, J. E., Linares, R. C., & Doering, P. J. (2003). Long coherence times at 300 K for nitrogen-vacancy center spins in diamond grown by chemical vapor deposition. Applied Physics Letters, 83(20), 4190–4192. https://doi.org/10.1063/1.1626791

Knauer, S., Hadden, J. P., & Rarity, J. G. (2020). In-situ measurements of fabrication induced strain in diamond photonic-structures using intrinsic colour centres. Npj Quantum Information, 6(1), Article 1. https://doi.org/10.1038/s41534-020-0277-1

Krushynska, A. O., Galich, P., Bosia, F., Pugno, N. M., & Rudykh, S. (2018). Hybrid metamaterials combining pentamode lattices and phononic plates. Applied Physics Letters, 113(20), 201901. https://doi.org/10.1063/1.5052161

Krödel, S., & Daraio, C. (2016). Microlattice Metamaterials for Tailoring Ultrasonic Transmission with Elastoacoustic Hybridization. Physical Review Applied, 6(6), 064005. https://doi.org/10.1103/PhysRevApplied.6.064005

Kushwaha, M. S., Halevi, P., Dobrzynski, L., & Djafari-Rouhani, B. (1993). Acoustic band structure of periodic elastic composites. Physical Review Letters, 71(13), 2022–2025. https://doi.org/10.1103/PhysRevLett.71.2022

Lavrentovich, O. D. (2012). Confocal Fluorescence Microscopy. In E. N. Kaufmann (Ed.), Characterization of Materials (1st ed., pp. 1–15). Wiley. https://doi.org/10.1002/0471266965.com127

Li, X., Xu, Z.-H., & Wang, R. (2006). In Situ Observation of Nanograin Rotation and Deformation in Nacre. Nano Letters, 6(10), 2301–2304. https://doi.org/10.1021/nl061775u

Li, Y., Baker, E., Reissman, T., Sun, C., & Liu, W. K. (2017). Design of mechanical metamaterials for simultaneous vibration isolation and energy harvesting. Applied Physics Letters, 111(25), 251903. https://doi.org/10.1063/1.5008674

Li, Y., Shen, Y., Cao, S., Zhang, X., & Meng, Y. (2019). Thermally triggered tunable vibration mitigation in Hoberman spherical lattice metamaterials. Applied Physics Letters, 114(19), 191904. https://doi.org/10.1063/1.5092423

Liu, Z., Zhang, X., Mao, Y., Zhu, Y. Y., Yang, Z., Chan, C. T., & Sheng, P. (2000). Locally Resonant Sonic Materials. Science, 289(5485), 1734–1736. https://doi.org/10.1126/science.289.5485.1734

Livengood, R., Tan, S., Greenzweig, Y., Notte, J., & McVey, S. (2009). Subsurface damage from helium ions as a function of dose, beam energy, and dose rate. Journal of Vacuum Science & Technology B: Microelectronics and Nanometer Structures Processing, Measurement, and Phenomena, 27(6), 3244–3249. https://doi.org/10.1116/1.3237101

Malik, I. A., & Barthelat, F. (2018). Bioinspired sutured materials for strength and toughness: Pullout mechanisms and geometric enrichments. International Journal of Solids and Structures, 138, 118–133. https://doi.org/10.1016/j.ijsolstr.2018.01.004

Malik, I. A., Mirkhalaf, M., & Barthelat, F. (2017). Bio-inspired “jigsaw”-like interlocking sutures: Modeling, optimization, 3D printing and testing. Journal of the Mechanics and Physics of Solids, 102, 224–238. https://doi.org/10.1016/j.jmps.2017.03.003

Mao, A., Zhao, N., Liang, Y., & Bai, H. (2021). Mechanically Efficient Cellular Materials Inspired by Cuttlebone. Advanced Materials, 33(15), 2007348. https://doi.org/10.1002/adma.202007348

Martínez-Sala, R., Sancho, J., Sánchez, J. V., Gómez, V., Llinares, J., & Meseguer, F. (1995). Sound attenuation by sculpture. Nature, 378(6554), 241–241. https://doi.org/10.1038/378241a0

Matache, L. C., Lixandru, P., Chereches, T., Mazuru, A., Chereches, D., Geanta, V., Voiculescu, I., Trana, E., & Rotariu, A. N. (2019). Determination of material constants for high strain rate constitutive model of high entropy alloys. IOP Conference Series: Materials Science and Engineering, 591(1), 012057. https://doi.org/10.1088/1757-899X/591/1/012057

Mavrikos, S., & Grigoropoulos, C. P. (2024a). Profile and microstructure accuracy of two-photon polymerization fabricated structures: The case study of the Phloeodes diabolicus. In R. Kling, W. Pfleging, & K. Sugioka (Eds.), Laser-based Micro- and Nanoprocessing XVIII (p. 24). SPIE. https://doi.org/10.1117/12.3002378

Mavrikos, S., & Grigoropoulos, C. P. (2024b). Tuning Young's modulus in multiphoton lithography. In A. V. Kabashin, M. Farsari, & M. Mahjouri-Samani (Eds.), Nanoscale and Quantum Materials: From Synthesis and Laser Processing to Applications 2024 (p. 12). SPIE. https://doi.org/10.1117/12.3005653

Meier, T., Li, R., Mavrikos, S., Blankenship, B., Vangelatos, Z., Yildizdag, M. E., & Grigoropoulos, C. P. (2024). Obtaining auxetic and isotropic metamaterials in counterintuitive design spaces: An automated optimization approach and experimental characterization. Npj Computational Materials, 10(1), 3. https://doi.org/10.1038/s41524-023-01186-2

Mirkhalaf, M., & Barthelat, F. (2017). Design, 3D printing and testing of architectured materials with bistable interlocks. Extreme Mechanics Letters, 11, 1–7. https://doi.org/10.1016/j.eml.2016.11.005

Mochalin, V. N., Shenderova, O., Ho, D., & Gogotsi, Y. (2012). The properties and applications of nanodiamonds. Nature Nanotechnology, 7(1), Article 1. https://doi.org/10.1038/nnano.2011.209

Neal, B. G. (1977). The plastic methods of structural analysis (3. (S.I.) ed). Chapman and Hall.

Olberding, J. (2021). The mechanical puzzle of crush-resistant beetles. Journal of Experimental Biology, 224(1), jeb235069. https://doi.org/10.1242/jeb.235069

Orloff, J., Swanson, L., & Utlaut, M. W. (2003). High resolution focused ion beams: FIB and its applications: the physics of liquid metal ion sources and ion optics and their application to focused ion beam technology. Kluwer Academic/Plenum Publishers.

Pan, F., Khan, M., Ragab, A. H., Javed, E., Alsalmah, H. A., Khan, I., Lei, T., Hussain, A., Mohamed, A., Zada, A., & Ansari, M. Z. (2023). Recent advances in the structure and biomedical applications of nanodiamonds and their future perspectives. Materials & Design, 233, 112179. https://doi.org/10.1016/j.matdes.2023.112179

Pertoldi, L., Zega, V., Comi, C., & Osellame, R. (2020). Dynamic mechanical characterization of two-photon-polymerized SZ2080 photoresist. Journal of Applied Physics, 128(17), 175102. https://doi.org/10.1063/5.0022367

Qureshi, A., Li, B., & Tan, K. T. (2016). Numerical investigation of band gaps in 3D printed cantilever-in-mass metamaterials. Scientific Reports, 6(1), 28314. https://doi.org/10.1038/srep28314

Ritchie, R. O. (2011). The conflicts between strength and toughness. Nature Materials, 10(11), 817–822. https://doi.org/10.1038/nmat3115

Rivera, J., Hosseini, M. S., Restrepo, D., Murata, S., Vasile, D., Parkinson, D. Y., Barnard, H. S., Arakaki, A., Zavattieri, P., & Kisailus, D. (2020). Toughening mechanisms of the elytra of the diabolical ironclad beetle. Nature, 586(7830), 543–548. https://doi.org/10.1038/s41586-020-2813-8

Roux, W. (2016). The LS-TaSCTM Multipoint Method for Constrained Topology Optimization.

Sepehri, S., Jafari, H., Mashhadi, M. M., Yazdi, M. R. H., & Fakhrabadi, M. M. S. (2020). Study of tunable locally resonant metamaterials: Effects of spider-web and snowflake hierarchies. International Journal of Solids and Structures, 204–205, 81–95. https://doi.org/10.1016/j.ijsolstr.2020.08.014

Serra, P., & Piqué, A. (2019). Laser-Induced Forward Transfer: Fundamentals and Applications. Advanced Materials Technologies, 4(1), 1800099. https://doi.org/10.1002/admt.201800099

Sheikh, H. M., Meier, T., Blankenship, B., Vangelatos, Z., Zhao, N., Marcus, P. S., & Grigoropoulos, C. P. (2022). Systematic design of Cauchy symmetric structures through Bayesian optimization. International Journal of Mechanical Sciences, 236, 107741. https://doi.org/10.1016/j.ijmecsci.2022.107741

Sheikh, H. M., Meier, T., Blankenship, B., Vangelatos, Z., Zhao, N., Marcus, P. S., & Grigoropoulos, C. P. (2022). Systematic design of Cauchy symmetric structures through Bayesian optimization. International Journal of Mechanical Sciences, 236, 107741. https://doi.org/10.1016/j.ijmecsci.2022.107741

Sigmund, O., & Maute, K. (2013). Topology optimization approaches: A comparative review. Structural and Multidisciplinary Optimization, 48(6), 1031–1055. https://doi.org/10.1007/s00158-013-0978-6

Singh, N. K., & Singh, K. K. (2015). Review on impact analysis of FRP composites validated by LS-DYNA. Polymer Composites, 36(10), 1786–1798. https://doi.org/10.1002/pc.23064

Stankevičius, E., Malinauskas, M., & Račiukaitis, G. (2011). Fabrication of Scaffolds and Micro-Lenses Array in a Negative Photopolymer SZ2080 by Multi-Photon Polymerization and Four-Femtosecond-Beam Interference. Physics Procedia, 12, 82–88. https://doi.org/10.1016/j.phpro.2011.03.109

Steinert, S., Dolde, F., Neumann, P., Aird, A., Naydenov, B., Balasubramanian, G., Jelezko, F., & Wrachtrup, J. (2010). High sensitivity magnetic imaging using an array of spins in diamond. Review of Scientific Instruments, 81(4), 043705. https://doi.org/10.1063/1.3385689

Stelzer, E. H. K., Strobl, F., Chang, B.-J., Preusser, F., Preibisch, S., McDole, K., & Fiolka, R. (2021). Light sheet fluorescence microscopy. Nature Reviews Methods Primers, 1(1), 73. https://doi.org/10.1038/s43586-021-00069-4

Stern, H. L., Gu, Q., Jarman, J., Eizagirre Barker, S., Mendelson, N., Chugh, D., Schott, S., Tan, H. H., Sirringhaus, H., Aharonovich, I., & Atatüre, M. (2022). Room-temperature optically detected magnetic resonance of single defects in hexagonal boron nitride. Nature Communications, 13(1), Article 1. https://doi.org/10.1038/s41467-022-28169-z

Surjadi, J. U., Gao, L., Du, H., Li, X., Xiong, X., Fang, N. X., & Lu, Y. (2019). Mechanical Metamaterials and Their Engineering Applications. Advanced Engineering Materials, 21(3), 1800864. https://doi.org/10.1002/adem.201800864

Tian, Y., Luković, M. K., Erps, T., Foshey, M., & Matusik, W. (2021). AutoOED: Automated Optimal Experiment Design Platform (Version 1). arXiv. https://doi.org/10.48550/ARXIV.2104.05959

Toyli, D. M., de las Casas, C. F., Christle, D. J., Dobrovitski, V. V., & Awschalom, D. D. (2013). Fluorescence thermometry enhanced by the quantum coherence of single spins in diamond. Proceedings of the National Academy of Sciences of the United States of America, 110(21), 8417–8421. https://doi.org/10.1073/pnas.1306825110

Tserevelakis, G. J., Tekonaki, E., Kalogeridi, M., Liaskas, I., Pavlopoulos, A., & Zacharakis, G. (2023). Hybrid Fluorescence and Frequency-Domain Photoacoustic Microscopy for Imaging Development of Parhyale hawaiensis Embryos. Photonics, 10(3), 264. https://doi.org/10.3390/photonics10030264

Vangelatos, Z., Sheikh, H. M., Marcus, P. S., Grigoropoulos, C. P., Lopez, V. Z., Flamourakis, G., & Farsari, M. (2021). Strength through defects: A novel Bayesian approach for the optimization of architected materials. Science Advances, 7(41), eabk2218. https://doi.org/10.1126/sciadv.abk2218

Wang, R. Z., Suo, Z., Evans, A. G., Yao, N., & Aksay, I. A. (2001). Deformation mechanisms in nacre. Journal of Materials Research, 16(9), 2485–2493. https://doi.org/10.1557/JMR.2001.0340

Weggler, T., Ganslmayer, C., Frank, F., Eilert, T., Jelezko, F., & Michaelis, J. (2020). Determination of the Three-Dimensional Magnetic Field Vector Orientation with Nitrogen Vacany Centers in Diamond. Nano Letters, 20(5), 2980–2985. https://doi.org/10.1021/acs.nanolett.9b04725

Wegst, U. G. K., & Ashby, M. F. (2004). The mechanical efficiency of natural materials. Philosophical Magazine, 84(21), 2167–2186. https://doi.org/10.1080/14786430410001680935

Wegst, U. G. K., Bai, H., Saiz, E., Tomsia, A. P., & Ritchie, R. O. (2015). Bioinspired structural materials. Nature Materials, 14(1), 23–36. https://doi.org/10.1038/nmat4089

Wickramasinghe, S., Al-Ketan, O., Peng, C., Tee, Y. L., Kajtaz, M., & Tran, P. (2023). Influence of design parameters on the flexural properties of a bio-inspired suture structure. Virtual and Physical Prototyping, 18(1), e2204845. https://doi.org/10.1080/17452759.2023.2204845

Wu, Y., & Weil, T. (2022). Recent Developments of Nanodiamond Quantum Sensors for Biological Applications. Advanced Science, 9(19), 2200059. https://doi.org/10.1002/advs.202200059

Yao, H.-B., Fang, H.-Y., Wang, X.-H., & Yu, S.-H. (2011). Hierarchical assembly of micro-/nano-building blocks: Bio-inspired rigid structural functional materials. Chemical Society Reviews, 40(7), 3764. https://doi.org/10.1039/c0cs00121j

Yaraghi, N. A., & Kisailus, D. (2018). Biomimetic Structural Materials: Inspiration from Design and Assembly. Annual Review of Physical Chemistry, 69(1), 23–57. https://doi.org/10.1146/annurev-physchem-040215-112621

Zeng, Q., Duan, S., Zhao, Z., Wang, P., & Lei, H. (2022). Inverse Design of Energy-Absorbing Metamaterials by Topology Optimization. Advanced Science, 10(4), 2204977. https://doi.org/10.1002/advs.202204977

Zheng, X., Smith, W., Jackson, J., Moran, B., Cui, H., Chen, D., Ye, J., Fang, N., Rodriguez, N., Weisgraber, T., & Spadaccini, C. M. (2016). Multiscale metallic metamaterials. Nature Materials, 15(10), Article 10. https://doi.org/10.1038/nmat4694

Ziegler, J. F., Ziegler, M. D., & Biersack, J. P. (2010). SRIM – The stopping and range of ions in matter (2010). Nuclear Instruments and Methods in Physics Research Section B: Beam Interactions with Materials and Atoms, 268(11–12), 1818–1823. https://doi.org/10.1016/j.nimb.2010.02.091

Žukauskas, A., Batavičiūtė, G., Ščiuka, M., Balevičius, Z., Melninkaitis, A., & Malinauskas, M. (2015). Effect of the photoinitiator presence and exposure conditions on laser-induced damage threshold of ORMOSIL (SZ2080). Optical Materials, 39, 224–231. https://doi.org/10.1016/j.optmat.2014.11.031